A THREE-PHASE STUDY ON PRE-FLUSH STAGE IN SANDSTONE ACIDIZING: EXPERIMENTAL AND MODELING ANALYSIS OF EVOLVED CO_2 IN A HYDROCARBON AND AQUEOUS ENVIRONMENT

A Dissertation

by

SAJJAAT MUHEMMED REYATH

Submitted to the Graduate and Professional School of
Texas A&M University
in partial fulfillment of the requirements for the degree of

DOCTOR OF PHILOSOPHY

Chair of Committee,	Hadi Nasrabadi
Committee Members,	Mahmoud El-Halwagi
	Jerome Schubert
	Tanya Wickliff
Head of Department,	Timothy Jacobs

December 2021

Major Subject: Interdisciplinary Engineering

ABSTRACT

Limited studies have been conducted in understanding the mechanics of pre-flush stages in sandstone acidizing processes. Amongst those conducted in this area, all efforts have been directed toward singular aqueous-phase scenarios. Encountering 100% water saturation (S_w) in the near-wellbore region is seldom the case, as hydrocarbons at residual or higher saturations can exist. Carbonate mineral dissolution, being the primary objective of the pre-flush stage, results in carbon-di-oxide (CO_2) evolution. This can lead to a multi-phase presence depending on the conditions in the porous medium, and this factor has been unaccounted for in previous studies under the assumption that all the evolved CO_2 is dissolved in the surrounding solutions. The performance of a pre-flush stage changes in the presence of multi-phase environments in the porous media.

A detailed study is presented on the effects of evolved CO_2 due to carbonate mineral dissolution, and its ensuing activity during the pre-flush stages in matrix acidizing of sandstone reservoirs. Carbon Tan sandstone cores were used toward the purpose of this study, of which two were fully water saturated, the remaining two were brought to initial water saturation (S_{wi}) and residual oil saturation to waterfloods (S_{orw}), prior to conducting pre-flush stage experiments. The pre-flush stage fluid, 15 wt% hydrochloric acid (HCl), was injected in the concerning cores while maintaining initial pore pressures of 1,200 psi and constant temperatures of 150°F.

In fully water saturated cores, a major fraction of un-reacted carbonate minerals still existed even after 40 pore volumes (PV) of pre-flush acid injection. Heterogeneity is induced as carbonate mineral dissolution progresses within the core, creating paths of least resistance, leading to

preferential flow of the incoming fresh acid. This leads to regions of carbonate minerals being untouched during the pre-flush stimulation stage. An average of 25% recovery of the oil in place was seen from pre-flush experiments conducted on cores with S_{orw}. In cores with S_{wi}, the oil saturation was reduced during the pre-flush stage to a similar value as in the cores with S_{orw}.

The potential of evolved CO_2, a by-product of the sandstone acidizing pre-flush stage, towards its contribution in swelling the surrounding oil and thus mobilizing the trapped oil has been depicted in this study.

DEDICATION

It is very difficult to connect the dots looking into future, hence I would like to dedicate my time at Texas A&M University to one God who planned and paved my way into this exciting field ofresearch. Finally, I would like to thank Dr. Hisham Nasr-el-Din who patiently taught me the fundamentals of research and inculcated the habit on relying on my myself first and then take help along the way.

ACKNOWLEDGEMENTS

I would like to thank my committee chair, Dr. Hadi Nasrabadi, and my committee members, Dr. El-Halwagi, Dr. Schubert, Dr. Wickliff for their guidance and support throughout the course of this research.

Thanks to my friends and colleagues and the department faculty and staff for making my time at Texas A&M University a great experience. Finally, thanks to my parents for their support and encouragement.

CONTRIBUTORS AND FUNDING SOURCES

Contributors

This work was supervised by a dissertation committee consisting of Professor Dr. Hadi Nasrabadi and Dr. Hisham of the Department of petroleum engineering, Dr. Halwagi of the Department of chemical engineering, Dr. Schubert of the Department of petroleum engineering and Dr. Wickliff of Department of engineering.

All other work conducted for the dissertation was completed by the student independently.

Funding Sources

Graduate study was supported by a fellowship from Texas A&M University. Its contents are solely the responsibility of the authors and do not necessarily represent the official views of the Department of engineering.

NOMENCLATURE

1D = one-dimensional

3D = three-dimensional

A_{eff} = weighted harmonic average cross sectional area in two consecutive grid blocks, ft^2

$C_{calcite}$ = concentration of solid mineral calcite, $lbmol/ft^3$

$C_{dolomite}$ = concentration of solid mineral dolomite, $lbmol/ft^3$

C_{HCl_aq} = concentration factor for aqueous species ‘HCl’, $lbmol/ft^3$

C_{s1} = concentration factor for solid species 'calcite’, $lbmol/ft^3$

C_{s2} = concentration factor for solid species 'dolomite’, $lbmol/ft^3$

D = effective dispersion coefficient, cm^2/s

dI = numerical model grid cell length in I direction, in.

dJ = numerical model grid cell length in J direction, in.

dK = numerical model grid cell length in K direction, in.

D_{ji} = dispersion coefficient of component 'i' in phase 'j', cm^2/min

E_{a1} = activation energy for HCl - Calcite reaction, BTU/lbmol

E_{a2} = activation energy for HCl - Dolomite reaction, BTU/lbmol

K_0 = initial grid block permeability, md

k_{abs} = absolute permeability, md

k_{eff} = weighted harmonic average absolute permeability in two consecutive grid blocks, md

k_{eo} = effective permeability to oil, md

k_{ew} = effective permeability to water, md

K_i = K-value of species 'i', dimensionless

k_{mul} = constant in exponential structure-property relationship, dimensionless

l_{eff} = weighted harmonic average nodal spacing between two consecutive grid blocks, ft

m = exponent in Carman-Kozeny structure-property relationship, dimensionless

n = concentration order for reacting component, dimensionless

N_g = Corey's gas curve exponent, dimensionless

N_o = Corey's oil curve exponent, dimensionless

N_w = Corey's water curve exponent, dimensionless

o_i = mole fraction of species 'i' in oil phase, fraction

PV = pore volume, dimensionless

q_{jk} = source / sink flow rates of phase 'j' in well layer '*k*', ft^3/min

R = universal gas constant, BTU/R-lbmol

r_k = volumetric rate of reaction 'k', lbmol/ft^3-s

Sa1 = reactive surface area per unit volume of calcite mineral, cm^2/cm^3

Sa2 = reactive surface area per unit volume of dolomite mineral, cm^2/cm^3

s_{ki} = reactant stoichiometric coefficient of species 'i' in reaction 'k'

s'_{ki} = product stoichiometric coefficient of species 'i' in reaction 'k'

S_{aq} / S_w = aqueous / water phase saturation, fraction

S_o = oil saturation, fraction

S_{orw} = residual oil saturation to waterflood, fraction

S_{wi} = initial water saturation, fraction

T_{abs} = absolute temperature, R

V_f = volume of fluids, ft^3

Vv = void volume, ft^3

w_i = mole fraction of species 'i' in aqueous phase, fraction

$x_{aq,HCl}$ = mole fraction of species 'HCl' in aqueous phase 'aq', fraction

y_i = mole fraction of species in vapor phase, fraction

Z = Z-factor, dimensionless

αi = relative volatility of species 'i' with respect to a reference

α = mechanical dispersion coefficient, cm

μ_{g-T} = gas phase viscosity – temperature-dependent component, cp

μ_{Li} = liquid phase viscosity of species 'i', cp

Φ = porosity, volume fraction

$\triangle j_{id}$ = concentration difference in mole fraction across nodes for species 'i' in phase 'j', fraction

$\triangle \varphi_{jd}$ = potential difference across nodes for phase 'j', atm

ρ_g = gas-phase mol density, lbmol/ft^3

ρ_{aq} /ρ_w = aqueous-phase mole density, lbmol/ft^3

ρ_{wi} = species 'i' aqueous phase mole density, lbmol/ft^3

ρ_{oi} = species 'i' oil phase mole density, lbmol/ft^3

$M\Omega$ = Mega Ohms

TABLE OF CONTENTS

Page

LIST OF FIGURES

FIGURE Page

LIST OF TABLES

TABLE Page

1. INTRODUCTION[*]

Matrix acidizing is the process of removing formation damage in the near-wellbore region thereby enhancing the near-wellbore permeability. More specifically, sandstone acidizing is aimed at improving permeability by dissolving carbonate and siliceous minerals like clays and feldspars. It is a three-stage sequential process: pre-flush stage aimed at removing carbonate minerals; main-treatment stage aimed at removing siliceous minerals; post-flush stage; to displace the reaction products farther away from the wellbore. During the pre-flush stage, a reactive acid, commonly HCl, is used to dissolve the carbonate minerals. This stage is essential as the presence of carbonate minerals during main-treatment, which is a mixture of hydrofluoric acid (HF) and HCl also known as mud acid, causes more damage due to the precipitation of calcium fluoride in the formation. A detailed explanation regarding each stage is given by (Williams et al. 1979).

The reaction of HCl with carbonate minerals generates CO_2, and the evolution of CO_2 changes the fluid flow characteristics in porous media (Shaughnessy and Kunze 1981). While most of the sandstone acidizing experiments at the laboratory scale focus on improving rock permeability by

---

[*] Part of this chapter is reprinted with permission from "A Three-Phase Study on Pre-Flush Stage in Sandstone Acidizing: Experimental and Modeling Analysis of Evolved CO_2 in a Hydrocarbon and Aqueous Environment" by S. Muhemmed, H.T. Kumar and H.A. Nasr-El-Din, 2019. 2019 SPE Annual Technical Conference and Exhibition, SPE-195897-MS, Copyright 2019 by SPE.

dissolving the clays and feldspars minerals in single-phase aqueous environments, very little work has been done to analyze the process in environments consisting of water and oil, as well as in quantifying and studying the effects of CO_2 liberated during the pre-flush. Aside from CO_2, the HCl/limestone reactions yield water and calcium chloride ($CaCl_2$), and the HCl/dolomite reactions yield water, $CaCl_2$, and magnesium chloride ($MgCl_2$) as products. These additional products influence the salinity, and thus alter the viscosities of the aqueous solutions in the porous media. This in turn influences the fluid-flow and CO_2 solubility dynamics. Abdulagatov and Azizov (2006) reported experimentally measured viscosities of $CaCl_2$ solutions at various concentrations, temperatures and pressures. Various saturation conditions exist in the field scenario. For example, an oil producing well would have the near wellbore region consisting of oil and initial water saturations, whereas, a water injection well would most likely have oil at residual conditions to a waterflood in the near wellbore region.

Although the success rate of sandstone acidizing is low due to the uncertainty associated with the fluid-formation interactions (Nasr-El-Din et al. 2007), the damage incurred by calcium fluoride precipitation can be greatly minimized if a sufficient amount of HCl is used to remove carbonate minerals. Another purpose of the pre-flush is to create a low-pH region in the near wellbore zone, for HF to successfully react with siliceous minerals. McLeod et al. (1983) suggested that pre-flush volumes of 122 gallons of 15 wt% HCl /ft would be required for 10 vol% of calcium carbonate present in a 15% porous formation. However, Hill et al. (1994) suggested that 25 to 50 gal of HCl/ft for pre-flush volumes are enough to prevent live HF from penetrating beyond the live HCl-front, for formations with calcium carbonate content up to 15 vol%. Exler et al. (2014) suggested empirical guidelines to select pre-flush volumes of 50 to 75 gal/ft based on solubility to HCl. However, their knowledge pool was limited to Central American and geothermal wells. Given that beds of varying permeability may exist in the vicinity of the wellbore, D. Fu (2010) invented a self-diverting pre-flush acid that can encompass a larger near wellbore area by plugging the high permeable zones and dissolving more carbonate minerals in the zones of interest.

The carbonate minerals form a major cementing material by volume in clastic reservoirs like sandstones (Zhixue et al. 2010). Although the carbonate mineral distribution in sandstones vary significantly, investigating its contribution to sandstone acidizing process and more specifically during pre-flush stage may assist to increase the overall performance of matrix acidizing. Previously, several mathematical models were developed to emulate the sandstone acidizing (Schechter and Gidley 1969; Hekim et al. 1982; Bryant 1993; Sevougian et al. 1995; Zhou et al. 2016; Leong et al. 2018). However, the models did not include the evolution of CO_2 because of calcite and dolomite dissolution. Zhou et al. (2016) conducted both experimental and simulation studies of sandstone acidizing. Nevertheless, calcite composition in the core sample was only around 3.1 wt%. Hence, the effect of resulting permeability change and CO_2 evolved was minimal. The carbonate mineral distribution in some sandstones go as high as 15 wt%. Their dissolution alters the porosity and permeability profile, and the generated CO_2 influences the fluid saturations in the near wellbore region. Hence, consideration of CO_2 during the analyses will give more representative results.

Akin and Kovscek (2003) provide an overview of X-ray CT technique as a powerful non-destructive imaging tool, helpful in acquiring porosity, permeability and fluid phases' distributions in porous media at the laboratory scale. Ali and Nasr-El-Din (2018) performed modeling studies in the area of carbonate acidizing at the laboratory scale, and matched the carbonate rock dissolution by quantifying the initial porosity distribution of the cores accurately via CT scans.

A three-phase flow numerical simulation model coupled with chemical reaction and structure property modeling features is used to validate the conducted pre-flush stage coreflood experiments. The workflow adopted to investigate the effect of CO_2 are as follows:

1. Cores scanned using Computed Tomography (CT)
2. Characterized initial porosity distributions across cores.
3. Experimentally quantified rock's carbonate mineral content - calcite and dolomite, using X-Ray Diffraction (XRD).
4. Populated measured distributions of porosities and mineral concentrations in core-representative models.
5. Measured calcium chloride and magnesium chloride, i.e. acid-carbonate mineral reaction products, and spent HCl concentrations in coreflood effluents.
6. Pressure drops across cores logged during tests.

7. Numerical model calibration performed via history matching with measured experimental parameters from corefloods.

8. Utilize calibrated numerical model to understand and analyze physics involved in this complex sub-surface process.

In the present study, a detailed investigation is performed via experimental analyses through corefloods and backed by modeling studies to evaluate the effects of CO_2 evolved during the sandstone acidizing process. Accounting for the complete mineral dissolution reactions, CO_2 evolution, and CO_2's subsequent behavior in the pre-flush stage, play an important role in quantifying the experimentally measured parameters. The compositional modeling technique of the pre-flush stage shown in this study help assess the best conditions to be able to maximize oil production while flowing back post well stimulation. The numerical model calibration is performed with precision, by incorporating CT scan-based porosities, rock mineralogy, and coreflood effluent concentration measurements. The numerical model hosts a Darcy-scale model for describing fluid flow in porous media, and is coupled along with chemical reaction features, phase-equilibria, and structure-property relationships, to accurately mimic the sandstone pre-flush experiments. A proper design of the pre-flush can help alleviate problems during the main-flush stage, and aid in tapping the potential of evolved CO_2 on improving oil recovery from the formation.

1.1 Background on Sandstone Acidizing

By dissolving the rock or developing new channels around the wellbore, well stimulation improves the flow of oil or gas from the reservoir (Schechter 1992; Schlumberger 2000; Crowe et al. 1992). Acidizing and hydraulic fracturing are the most widely used stimulation methods. Hydraulic fracturing involves injecting fluids at a higher pressure than the formation pressure to produce channels/fractures through the formation, allowing for increased oil or gas production (Halliburton 2000c). Acids have been added to the sandstone and carbonate formations to enhance permeability and porosity around the well bore during acidizing (Economides and Nolte 2001; Halliburton 2000a, b). These acids can dissolve minerals found in reservoir rocks such as quartz, carbonates, and feldspar, improving permeability and, as a result, the flow rate of hydrocarbon fluid from the wellbore. In sandstone stimulation, each of these procedures (fracturing and acidizing) have their unique set of benefits and drawbacks. The decision to fracture or acidize a sandstone reservoir is influenced by a number of factors, including formation geology, production history, and well intervention goals (Al-Harthy et al. 2008/2009). In contrast to a tight formation with low porosity and permeability, which requires hydraulic fracturing, a formation with high permeability and porosity typically does not require fracturing. When exposed to hydraulic fracturing, a weakly connected deposit is more likely to collapse owing to overburden pressure. In addition, instead of matrix acidizing, hydraulic fracturing should not be used to stimulate damaged formations caused by drilling and production processes. Acid fracturing works best in carbonate rocks with a lot of spontaneous cracks and a lot of permeability (Qiu et al. 2014). The primary goal of sandstone matrix acidization is to dissolve/remove siliceous particles (clay, feldspar, and quartz) that obstruct hydrocarbon flow and diminish permeability around the wellbore (Crowe et al. 1992; Lindsay 1976). Injections of hydrofluoric acid (HF acid) or its precursors can do this (Kalfayan and Metcalf 2001; Kalfayan 2008). Following its discovery in 1935, HF acid was widely used on sandstone formations to repair damage and alleviate difficulties connected to sandstone drilling and production damage. Initially, this acid's primary use was to remove the mud filter cake, but it is currently used to solve a variety of issues, including the removal of siliceous particles and damage surrounding the wellbore. When it came to treating sandstone formations with a tiny quantity of calcium minerals, this acid proved to be highly effective. Because, only the fluoride ion (F^-) can react with silica and clay, sandstone formation components such as sand grains, feldspar, and clays react with HF acid. The reactive behavior of HF acid with silica, as demonstrated by Smith and Hendrickson (1965), makes it ideal for sandstone acidizing. Smith and Hendrickson demonstrated that hydrochloric, sulfuric, and nitric acids do not efficiently react with the sandstone formation (1965). Dowel came up with the notion of combining HCl and HF acids to prevent reaction products from precipitating in 1940. Smith and Hendrickson (1965) and Abdelmoneim and Nasr-El-Din (1965) documented injecting mud acid with a concentration of 3 percent HF and 12 percent HCl in sandstone acidizing (2015). Because of the many phases of fluids and their interactions with the minerals in the porous medium, acidizing sandstone is a tough and hard operation. Precipitation processes can occur as a result of fluid–mineral interactions, which can lower reservoir permeability. Due to multiple stages of fluids-formation reactions during sandstone acidizing, the success rate to remove the damage is generally not according to the requirement. Precipitation reactions may occur during sandstone acidizing, resulting in formation degradation and decrease in sandstone matrix as detailed by Al-Harthy (2008/2009). Sandstone reservoir frameworks are generally composed up of quartz grains cemented together by carbonates (A), quartz (B), and feldspar overgrowth (C). Pore-filling clays such as kaolinite (D) and pore-lining clays such as illite (E) reduce porosity.

$$4HF + SiO_2 \longrightarrow SiF_4 + 2H_2O$$

Silicon tetra fluoride (SiF_4) is a soluble gas that may undergo additional reactions when kept in solution by pressure, exactly as CO_2. Fluoride Ion (F-) is present in some form in the acids used to promote Sandstone formations. It is a highly reactive ion and the sole chemical that has a substantial reaction with sand and clay (Smith and Hendrickson, 1965). As soon as HF acid reaches a sandstone rock, it begins dissolving minerals. The pace at which minerals react with acid and the amount of exposed surface area determine how quickly they react and dissolve. The minerals in sandstone are classified into two types: slow and rapid reactive. Quartz reacts slowly, but feldspars and clays react quickly (Ponce da Motta et al. 1992).

2. EXPERIMENTAL PROCEDURES[*]

2.1 Materials

Four cylindrical cores of 6 in. length and 1.5 in. diameter were cut from Carbon Tan outcrop sandstone rocks. The mineralogy of the Carbon Tan rock, as obtained from X-Ray Diffraction (XRD) analysis, is listed in Table 1. 10 wt% potassium chloride (KCl) solution was used for saturating the cores. The brine was prepared by mixing KCl crystals of 98% purity obtained from a local company, with de-ionized (DI) water having a resistivity of 18.2 MΩ.cm. For the acid system used in the pre-flush stage, a 15 wt% HCl solution was prepared by diluting an industry grade concentrated HCl solution of 37 wt%. The base fluid used for dilution was 10 wt% KCl brine, and an industry grade corrosion inhibitor, 1% by volume, was added. A light, dead crude-oil sample of 41 °API, obtained from the Katz field in North Texas, was used for the hydrocarbon phase. The brine viscosity and density at 150°F and 14.7 psi were measured to be 0.56 cp and 1.054 g/cm3, respectively.

---

[*] Part of this chapter is reprinted with permission from “A Three-Phase Study on Pre-Flush Stage in Sandstone Acidizing: Experimental and Modeling Analysis of Evolved CO_2 in a Hydrocarbon and Aqueous Environment” by S. Muhemmed, H.T. Kumar and H.A. Nasr-El-Din, 2019. 2019 SPE Annual Technical Conference and Exhibition, SPE-195897-MS, Copyright 2019 by SPE.

Table 1—Mineralogy of the Carbon Tan rock, as obtained from X-Ray Diffraction (XRD) analysis.

Mineral	Concentration (wt%)
Quartz	85.0
Calcite	8.1
Kaolinite	1.5
Illite	2.3
Dolomite	3.1

2.2 Acid-Oil Compatibility Test

An acid-crude oil compatibility test was necessary to evaluate any potential sludge or emulsion formation. The compatibility test was performed by mixing 50 cm^3 of the acid system and 50 cm^3 of the crude oil in an autoclave vessel, with a magnetic stirrer in place. The fluids in the vessel were pressurized to 1,200 psi using N_2, and then heated to and maintained at 150°F via a magnetic hot plate. The contents were stirred at 500 rpm for 30 minutes. After the test, the autoclave vessel was depressurized. The contents were immediately deposited into a glass beaker for observation.

A sharp interface was noted between the crude oil and acid system immediately after transferring the contents from the autoclave vessel to a glass beaker. The final volumes of the two fluids were intact. No sludge or emulsions were observed. Thus, the acid system and crude oil were compatible.

2.3 Fluids Characterization

The crude oil was necessary to be studied and characterized in order to be able to understand its behavior, and its influence on the performance during the preflush stage. Kumar et al. (2020) measured the composition of the crude oil sample obtained from the Katz field in west Texas experimentally, using the gas chromatography technique. They also conducted experimental measurements of the crude oil's densities and viscosities with respect to temperatures, at atmospheric pressures. These measured attributes were later used toward creating a fluid model representative of the crude oil.

2.4 Computed Tomography (CT) Scans

The cores were characterized via CT scans, to acquire the initial porosity distributions across the core to a detailed level in accuracy. A laboratory grade CT scanner was used toward this purpose. Akin and Kovscek (2003) provide the methodology to acquire porosity distributions and fluid saturations in the porous media. Characteristic CT numbers, CT number, that are functions of attenuation coefficients, are assigned to a voxel on an arbitrary scale. The attenuation coefficients are specific for each material, i.e., rock and fluid types.

2.5 Coreflood Setup

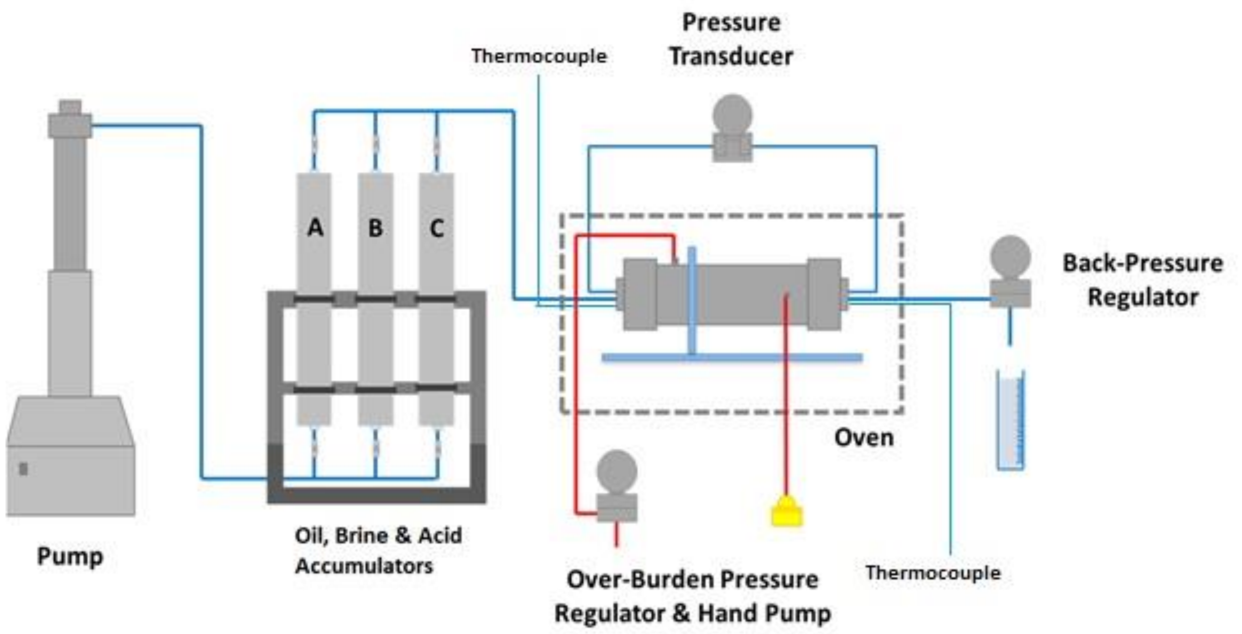

Fig. 1—A schematic diagram of laboratory coreflood setup used in the experimental study.

Fig. 1 shows a schematic of the coreflood setup. The system consisted of the following parts:

1. A precision syringe pump, with a maximum injection pressure specification of 2,000 psi (Teledyne ISCO 2018).
2. Three accumulators to hold the acid system, crude oil, and 10 wt% KCl brine.
3. Pressure transducer to measure the pressure drop across the core.
4. Overburden pump to apply overburden pressure by pumping hydraulic oil onto the rubber sleeve containing the core sample.

5. Backpressure regulator to apply the necessary initial pore pressure and the pressure at the core outlet, using nitrogen (N_2).

6. Corrosion resistant lines made of Hastelloy-B alloy, for transmitting injection and production fluids.

7. Hastelloy core holder contained within an oven, to apply the necessary reservoir temperature.

8. Thermocouples at the inlet and outlet, to measure fluids' temperatures while fluids enter and exit the core.

9. A commercial data acquisition software to record data and set control parameters (National Instruments 2003).

2.6 Syringe Pump

The acid system was injected into the core using a Teledyne ISCO D-series D1000 precision syringe pump with a maximum allowed working pressure of 2,000 psi.

2.7 Core Holder

Cores with a diameter of 1.5 inches and a length of 6 inches were operated using a core holder with a pressure range of 3,000 psi. A heat jacket was put around the core holder to heat the cores to the various testing temperature. The temperature was controlled by the oven in which the coreholder is placed. During the heating period, water was pumped at a rate of 2 cm^3/min. During the tests, a digital pressure transducer tied to a computer that runs LabView® software was employed to control and record the pressure reduction across the core.

Fig. 2–CT-scanner used to characterize cores.

The dissolution patterns generated in the Standstone cores were analyzed using a state-of-the-art Toshiba Aquilion RXL CT scanner (**Fig. 2**) with 3D sophisticated visualization software. This unit offers a 16-detector row 32-slice computerized tomography system that can reconstruct 0.5 mm data sets at up to 16 frames per second. The scanner features a 72 cm gantry opening with a +/-30-degree tilt and a high-resolution 0.5 mm x 16-row detector. In addition, the CT-contrast Scanner's resolution is just 2 mm at 0.3 percent.

2.8 Inductively Coupled Plasma Optical Emission Spectrometry (ICP-OES)

The concentration of various multivalent ions in the core effluent samples collected from the various coreflood experiments was determined using the Optima 7000 DV ICP-OES equipment (**Fig. 3**). Ca^{2+} and Mg^{2+} were two of the most often detected ions.

Fig. 3–Inductively Coupled Plasma Optical Emission Spectrometry (ICP-OES).

2.9 X-Ray Fluorescence (XRF)

The emission of distinctive "secondary" (or fluorescent) X-rays from a material that has been stimulated by high-energy X-rays or gamma rays is known as X-ray fluorescence (XRF). The rock samples are subjected to elemental and chemical analysis. A S2 Ranger X-Ray Fluorescence (XRF) equipment was utilized for regular, non-destructive chemical analysis of carbonate rock samples during this study (**Fig. 4**).

Fig. 4–S2 Ranger X-Ray Fluorescence (XRF).

2.10 Preparation of Cores

The sandstone cores, I, II, III and IV, were dried in an oven for 24 hours at 150°F, and the dry weights were recorded. The cores were then vacuumed with 10 wt% KCl solution for six hours. To ensure complete water saturation, the cores were loaded horizontally onto the coreflood system, and injected with brine at multiple rates, and assessed for stability in the pressure drop measurements at each rate. The pore volumes were estimated using the saturation method. The permeabilities to brine were then measured at room temperature, 1,200 psi backpressure, and 2,000 psi overburden pressure. Cores I and II were maintained at 100% S_w for the pre-flush stage.

Rivet et al. (2010) and Hendraningrat et al. (2013) performed drainage and imbibition experiments on Berea sandstone core plugs by using coreflood systems, in order to bring their cores to initial water saturations and residual oil saturations to waterfloods respectively. Using similar conditions as in the permeability measurements, for cores III and IV, the core holder was then shifted to a vertical posture, and the drainage experiments were performed by injecting crude oil from the top. The crude oil injection rates used were 0.1, 0.3, 0.5, 1 and 3 cm^3/min, in the stated order, with at least 2 pore volumes (PV) of injection per rate, and ensuring no more water was produced at each rate. Finally, the oil was injected at a maximum possible pressure below that of the overburden, to ensure no further water production was observed. The core holder was then brought back to the horizontal orientation while maintaining the same pressure and temperature conditions, and the effective permeability to oil (K_{eo}) at S_{wi} was measured.

Core IV was then oriented vertically at the same conditions, and injected with brine from the bottom, following a similar pattern in injection as that of the drainage experiments. This was followed until no more oil production was seen, rendering core IV at S_{orw} conditions. Table 2 shows the petrophysical properties of the cores.

Table 2—Petrophysical properties of the cores. *The oil recovery factor in core IV based on waterflooding, to bring the core to residual conditions, was 54% of the original oil in place.

Core	**Saturation**	**Absolute Permeability (md)**	**Porosity (%)**	**K_{eo} @ S_{wi}**	**K_{ew} @ S_{orw}**	**S_{wi}**	**S_{orw}**
I	100% Brine Saturated	14	13	-	-	-	-
II	100% Brine Saturated	15	13	-	-	-	-
III	**Initial Water**	14	12	8.2	-	0.39	-
IV	Residual Oil	15	13	-	4.4	-	0.29*

3. MODELING STUDIES[*]

3.1 Model Features

The approach by Kumar et al. (2019) was adopted in this study, for modeling the grid systems, structural property changes, fluid phase equilibria, and chemical reaction features. This methodology is extended toward a three-phase system comprising oil, aqueous and gaseous phases. A commercial compositional finite-difference reservoir simulator was used to design the reservoir models at a core scale, and perform numerical simulations to mimic the pre-flush stage experiments, in order to better comprehend the physics involved (CMG-STARS 2017).

3.2 Grid Domain

A 3D cuboidal Cartesian model, oriented at 152 x 25 x 25 grid cells in the I x J x K directions was built. The porosity-permeability structure relations provides the structure property relations used to model the dynamic permeability changes with that of the porosities, due to mineral dissolution from the acidizing process. The porosity-permeability structure property relations at

---

[*] Part of this chapter is reprinted with permission from “A Three-Phase Study on Pre-Flush Stage in Sandstone Acidizing: Experimental and Modeling Analysis of Evolved CO_2 in a Hydrocarbon and Aqueous Environment” by S. Muhemmed, H.T. Kumar and H.A. Nasr-El-Din, 2019. 2019 SPE Annual Technical Conference and Exhibition, SPE-195897-MS, Copyright 2019 by SPE.

the pore-scale level, used in the overall species conservation equation, are shown in Eqs.1 and 2. Eq.1 is known as the Carman-Kozeny relation and is used in model initialization.

$$K(\Phi) = K_0 \; [\Phi / \Phi_0]^m \; [(1 - \Phi_0)/(1 - \Phi)]^2 \text{ , } \ldots\ldots(1)$$

Where Φ_o is the mean porosity, K_0 represents the average permeability, taken as the value from the absolute permeability values measured in the conducted experiments, and the exponent 'm' is a constant, and is obtained via the history matching of absolute permeability experiments.

The permeability changes with the instantaneous change in the porosity due to the mineral dissolution, during acidizing the porous media, and this is captured in the numerical model by an exponential relation, as shown in Eq. C-2 (CMG STARS 2017).

$$k = K_0 \; e^{[k_{mul} \; (\Phi - \Phi_0)/(1 - \Phi_0)]} \text{ , } \ldots\ldots(2)$$

where k_{mul} is a constant, and is used as a history matching parameter in the simulations.

3.3 Fluid Domain

For the aqueous phase, five components were defined, namely: water, HCl, $CaCl_2$, $MgCl_2$, and $CO_{2\text{-}w}$ (water soluble fraction of CO_2). For the hydrocarbon phase, five components were defined, namely CO_2-o (oil soluble fraction of CO_2) and four lumped components representing the crude oil used in this study. The crude oil composition and lumping process is discussed later. A fraction of CO_2 may exist in the gaseous phase depending on the local pressure, temperature and salinity conditions.

To account for the presence of CO_2 in multi-phase environments, the phase equilibrium is modeled via thermodynamic *K*-Value relations.

The phase equilibrium is modeled through thermodynamic *K*-Value relations. For any given species 'i' that is soluble in the aqueous phase, the *K*-value is defined as $K_i = y_i/l_i$, where y_i is the mole fraction of species 'i' in the gaseous phase, and l_i is the mole fraction of species 'i' in the corresponding liquid phase, i.e., aqueous or oil phase, in which the species 'i' is soluble. For multi-component mixtures, the relative volatility of any component 'i', with respect to a reference component 'c' is defined by below Eq. 3

$$\alpha_i = \frac{yi/\boldsymbol{li}}{yc/\boldsymbol{lc}} = \frac{Ki}{Kc} \quad \text{(3)}$$

Reid et al. (1987) provide semi-empirical relations as functions of pressures and temperatures to estimate the K-Values for several pure components, as shown in Eq. 4. The gaseous-liquid *K*-Value correlation is used for the water component in the aqueous phase, and for the four lumped crude oil components and CO_2-o in the oil phase.

$$K = \left(\frac{\mathrm{KV_1}}{\mathrm{P}}\right) \mathrm{e}^{\mathrm{KV_4/(T-KV_5)}}, \quad \text{(4)}$$

where P is the pressure in psi, and T is the temperature in °F. **Table 3** provides values for KV_1, KV_4 and KV_5 for the pure components, as given by Reid et al. (1987), and those given for the lumped crude oil components were estimated by weighted-averaging the corresponding pure hydrocarbon component values with that of their mole fractions.

Table 3—*K*-values were obtained from Reid et al. (1987) for water and $CO_{2\text{-}o}$, and generated via weighted-averaging for the lumped crude oil components.

Component	**KV_1**	**KV_4**	**KV_5**
Water	1.7202E+06	-6,869.59	-376.64
$CO_{2\text{-}o}$	1.2504E+08	-5586.10	-459.38
IC4-NC5	3.664E+05	-5429.70	-459.67
FC6-FC14	6.684E+05	-7856.30	-459.67
FC15-FC20	2.753E+06	-12760.70	-459.67
FC21-FC38	6.977E+06	-15979.80	-459.67

For $CO_{2\text{-w}}$, an analytical model by Zhao et al. (2014) is used toward determining the maximum solubility of CO_2 in the aqueous phase, as a function of local temperature, pressure and salinity. Upon acquiring the maximum solubility of $CO_{2\text{-w}}$, a corresponding *K*-value is calculated to mimic the solubility conditions, and used by the simulator, thus adhering to the physical limit.

The *K*-value feature used by the numerical model, helps estimate effective viscosities and densities of the liquid mediums, based on the dynamically varying compositions.

For all the aqueous components, the values of their molecular weights are input to account for the material balance of all species during the simulations. Properties of the aqueous phase and solid mineral components are provided in **Table 4**

Table 4—Properties of aqueous phase components, used as inputs in the present numerical model.

Property	**Water**	**HCl**	**$MgCl_2$**	**$CaCl_2$**	**$CO_{2\text{-}w}$**	**Dolomit**	**Calcite**
Molecular Weight, lb/lbmol	18.02	36.5	95.21	110.98	44.01	184.40	100
Critical pressure,[a] psi	3198	3198[b]	3198[b]	3198[b]	1071	-	-
Critical temperature,[b] °F	705.47	705.47[b]	705.47[b]	705.47[b]	87.98	-	-
Density,[c] lb/ft^3	62.4	62.4[b]	144.83	134.22	0.113	177.29	169.18
Compressibility,[d] psi^{-1}	3E-06	3E-06[b]	3E-06[b]	3E-06[b]	e	1E-06	1E-06

a. Values obtained from Reid et al. (1987).

b. Values of defined components in the aqueous-phase equated to corresponding property of water, as it constitutes the majority of the phase.

c. Values at a reference pressure of 14.7 psi and a reference temperature of 72°F.

d. Values obtained from generic assumptions for water and rock by Dake (1978), defined in the present numerical model for a constant temperature of 72°F.

e. Value calculated based on mixing rule and Z-factor determination methodology by Redlich and Kwong (1949).

Likewise, **Table 5** provides the properties generated for the oil phase components based on the lumping schemes applied.

Table 5—Properties of oil phase components generated via lumping schemes, and used as inputs in the present numerical model.

Property	**$CO_{2\text{-}o}$**	**IC4-FC5**	**FC6-FC14**	**FC15-FC20**	**FC21-FC38**
Molecular Weight, lb/lbmol	44.01	69.79	116.59	245.34	343.25
Critical pressure, psi	1071	499.84	411.14	233.73	172.79
Critical temperature, °F	87.98	363.35	602.91	901.63	1047.01
Density, lb/ft^3	0.113	39.2	47.4	52.8	54.6
Compressibility,psi^{-1}	a	1.482E-05	7.934E-06	4.404E-06	4.778E-06

a. Value calculated based on mixing rule and Z-factor determination methodology by Redlich and Kwong (1949).

Aqueous/Oil phase viscosities are computed via standard correlations for Newtonian fluids as a function of temperature. The correlation for pure component viscosities for the liquid phases, provided by Reid et al. (1987), is shown in Eq. 5

$$\mu_{li} = avisc_i \, e^{[bvisc_i/T_{abs}]}, \ldots\ldots(5)$$

where μ_{li} is the corresponding liquid phase viscosity of component 'i' in cp, and T_{abs} is the absolute temperature in R. For the aqueous phase, the values of the constants, *avisc* and *bvisc*, for water, CO_2, $CaCl_2$ and $MgCl_2$ are given in Table 6. The values of these constants for the lumped crude oil components are generated via the lumping schemes, and Table 7 provides the constants for oil phase components.

Table A-6—Constants in Eq. 5 that were used as input in the numerical model, for the aqueous components.

Component	**avisc, cp**	**bvisc, R**
Water	**0.0047352**	**2,728.2**
CO_2	**0.0007573**	**2,395.9**
$CaCl_2$	**0.0973568**	**2,900.0**
$MgCl_2$	**0.0973568**	**2,900.0**

Constants for water and CO_2 were obtained from Reid et al. (1987). Constants for $CaCl_2$ and $MgCl_2$ were calibrated inputs, based matching the viscosities of experimentally measured saline solutions by Abdulagatov and Azizov (2006).

Table 7—Constants in Eq. 5, generated via lumping schemes, that were used as inputs in the numerical model for the oil phase components

Component	avisc, cp	bvisc, R
$CO_{2\text{-}o}$	0.0007573	2395.9
IC4-FC5	0.2405	495.78
FC6-FC14	0.2259	748.72
FC15-FC20	0.1517	1305.29
FC21-FC38	0.1184	1683.01

An effective liquid phase viscosity is then calculated by summing the products of mole fractions and viscosities of the individual components in the corresponding liquid phase, as given by Eq. 6 **(CMG STARS 2017).**

$$\mu_l = \sum_{i=1}^{n_c} \mu_{li}\ l_i\ , \qquad (6)$$

where μ_l represents the effective liquid phase viscosity, l_i represents the mole fraction of component i in the liquid phase, i.e. aqueous or oil phase, and n_c is the number of component in the corresponding liquid phase (6 in the aqueous phase, and 5 in the oil phase for the present study).

For water and $CO_{2\text{-w}}$, the correlation constants in Eq. 5 were directly obtained from Reid et al. (1987). For $CaCl_2$ and $MgCl_2$, the correlation constants in Eq. 5 were calibrated in a manner such that the viscosity model made close predictions to the experimentally measured viscosities of saline solutions by Abdulagatov and Azizov (2005), at different temperatures and atmospheric pressures.

The gaseous phase mole density was calculated using Eq.7.

$$\rho_g = \frac{P}{R\ Tabs\ Z}, \qquad (7)$$

where, ρ_g = gas phase mole density in lbmol/ft^3, P = ambient pressure in psi, T_{abs} = absolute temperature in R, and R = universal gas constant in BTU/R-lbmol. The Z-factor is calculated based on the methodology described by Redlich and Kwong (1949). Gaseous phase viscosity is initially calculated as a function of temperature using Eq. 8.

$\mu_{g-T} = 0.0136 + 3.80\ \mathrm{E} - 05\ \mathrm{T}$, ...(8)

where, μ_{g-T} = the temperature-dependent component of the gaseous-phase viscosity in cp, and T = temperature in °C. To represent gas viscosity variations with pressure, the value obtained from Eq. 6 undergoes a correction factor, as per the method suggested by Dean and Stiel (1965).

For CO_2-in-aqueous and CO_2-in-oil systems, the corresponding effective liquid density is calculated using Eq. 9 (Sandler 1977).

$\frac{1}{\rho_l} = \sum_{i=1}^{n_c} \frac{l_i}{\rho_{li}}$, ...(9)

where ρ_l = liquid phase (aqueous or oil) density in $lbmol/ft^3$, and ρ_{li} = mol density of species 'i' in liquid phase (aqueous or oil) in $lbmol/ft^3$.

3.4 Well Domain, Initial and Boundary Conditions

The injector is located at the inlet face, namely at grid cell locations with I=152, and the producer is located at the outlet face, namely at grid cell locations with I=1. Fig. 5 depicts the inlet/outlet device in the coreflood apparatus, and the corresponding grid-perforations at the inlet/outlet faces established in the numerical model. The controls of the injector and producer are similar to those followed in the experiments. The injector is controlled by injection rates, and the producer is controlled by a constant pressure of 1,200 psi, similar to the back pressure used in the experiments.

The model is initialized with inputs to all grid cells at 1,200 psi pressures, a constant temperature set at 150°F, and the appropriate initial fluid saturations representative of the cores being modeled.

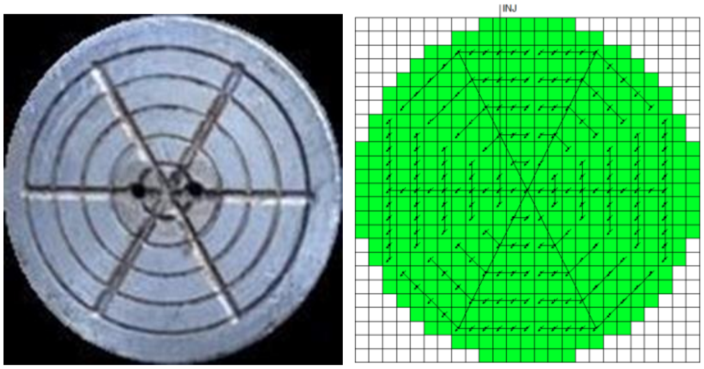

Fig. 5— (Left) A photo of the inlet/outlet device in the coreflood, consisting of two spouts, one through which fluids enter the core, and the other through which fluids reach the pressure transducer. Straight and concentric cavities through and around the spouts enable fluid transmission across the core face. (Right) The numerical model's inlet/outlet faces portraying the corresponding grid perforations, to mimic the experimental device. Grid cells marked in green are active and take part in the simulations, the black dots on the grid cells indicate perforations, and the blank grid cells are inactive, i.e., they do not take part in the simulations.

3.5 Rock-Fluid Interaction Parameters

Two chemical reactions, namely HCl-calcite and HCl-dolomite, are modeled based on the given chemical reactions in Eq. 10 and 11.

$CaCO_3(s) + 2\,HCl(aq) \rightarrow H_2O(aq) + CO_2(g/l/sc) + CaCl_2(aq)$, ……………..……...……...(10)

$CaMg(CO_3)_2\,(s) + 4\,HCl(aq) \rightarrow 2H_2O(aq) + 2CO_2(g/l/sc) + CaCl_2(aq) + MgCl_2(aq)$, ..…....(11)

where (s) represents the solid phase and (aq) indicates the aqueous phase. (g), (l) and (sc) represent the gaseous, liquid, and supercritical phases respectively, which are the possible states in which the evolved CO_2 that remains as a separate fraction may exist in. In modeling these chemical reactions, the concentrations of acid species are represented by Eq. 3, and that of calcite and dolomite minerals are represented by Eqs. 12 and 13.

$C_{HCl\_aq} = S_{aq}\,(\rho_{aq}\,x_{aq,HCl})^{n1}$,…………………....……………………………………….(12)

where C_{HCl_aq} is the reaction order applied concentration factor for the concentration of acid species 'HCl' in aqueous phase 'aq' in lbmol/ft^3, S_{aq} represents the aqueous phase 'aq' saturation, ρ_{aq} represents the effective aqueous phase density in lbmol/ft^3, $x_{aq,HCl}$ represents mole fraction of acid species 'HCl' in the aqueous phase 'aq', and n1 represents the reaction order applied to the acid species concentration.

$C_{S1} = (C_{calcite})^{n2}$……………..........................………………......………….……..…………(13)

$C_{S2} = (C_{dolomite})^{n3}$, ……………………………………………………………………(14)

where C_{S1} represents the reaction order applied concentration factor for calcite concentration, $C_{calcite}$ (in lbmol/ft^3), and C_{S2} represents the reaction order applied concentration factor for dolomite concentration, $C_{dolomite}$ (in lbmol/ft^3), with the corresponding species reaction orders of the minerals being n2 and n3. The volumetric reaction rates are modeled for calcite and dolomite dissolution, as shown in Eqs. 15 and 16 respectively.

$r_1 = A_1 \ e^{(-Ea1/(T_{abs} R)} \ Sa1 \ \Phi f \ C_{HCl\_aq} \ C_{S1}$, ………………………………………………(15)

$r_2 = A_2 \ e^{(-Ea2/(T_{abs} R)} \ Sa2 \ \Phi f \ C_{HCl\_aq} \ C_{S2}$, ………………………………………………(16)

where 'A' is the frequency factor, 'Ea' is the activation energy, 'Sa' is the reactive surface area of the mineral per unit reaction volume, 'Φ_f' represents the current fluid phase porosity in the porous medium, and R is the universal gas constant. Attributes with '1' represent that of HCl-calcite interaction, and those with '2' represent that of HCl-dolomite interaction. In this study, the products ($A_1 \ e^{(-Ea1/Tabs R)}$ Sa1) and ($A_2 \ e^{(-Ea2/Tabs R)}$ Sa2) are lumped together as the average volumetric reaction rate constants, K_1 and K_2, respectively. The values of K_1 and K_2 are determined via history matching the numerical model with that of experimental data, as shown in the subsequent sections.

The acid species transport mechanisms are described via diffusion and dispersion mechanisms in the model

Fig. 6 depicts the phase diagram for CO_2, (Cheng et al. 2017). CO_2's critical point is defined at 87.98°F and 1,071 psi. At the tested pore pressures of 1,200 psi and temperature of 150°F, CO_2's state of aggregation lies at the border of the gas-supercritical line. A three-phase relative permeability formulation is used for representing multi-phase flow in a water-wet rock system, and is provided in Appendix B. Since majority of the sandstone reservoirs in the world are water-wet (Zimmerle 1995), it is assumed that the un-aged sandstone cores used in this study were of similar nature.

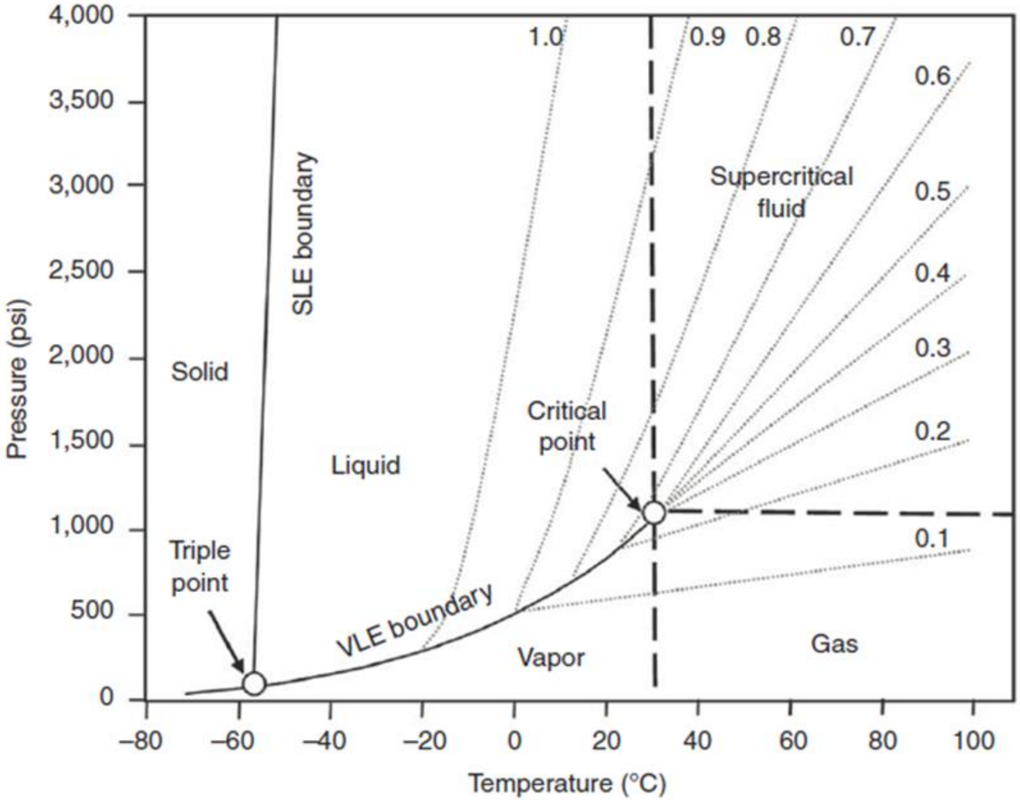

Fig. 6—CO2 phase diagram, showing states of pure CO2 with respect to temperature and pressure. SLE = solid/liquid equilibrium, VLE = vapor/liquid equilibrium (after Cheng 2017).

3.6 Fluid Flow and Species Conservation

A Reaction-Advection-Dispersion model is used to describe the pre-flush stage acidizing process in sandstones. The species conservation equation for an oil/water/gas/solids system is provided in Eqs. 17 through 20, and portray the Darcy-scale fluid-flow coupled with that of chemical reactions.

$$\frac{\partial}{\partial t}[V_f\ (\rho_w S_w\ w_i\ +\ \rho_g\ S_g\ y_i\ +\ \rho_o S_o\ o_i)\ ] =$$

{Accumulation Terms for Flowing Components in aqueous, gaseous and oil phases}

$$\sum_{d=1}^{n_f}[\, T_{wd}\ \ \rho_w\ \ w_i\ \ \triangle\,\phi_{wd}\ +\ T_{gd}\ \ \rho_g\ \ y_i\ \triangle\,\phi_{gd} +\ T_{od}\ \ \rho_o\ \ o_i\ \triangle\,\phi_{od}\,]\ \ +$$

{Darcy Flow Terms in aqueous, gaseous and oil phases}

$$V\ \sum_{k=1}^{n_r}\ (s'_{ki}\ -\ s_{ki})\ r_k\ +$$

{Chemical Reaction Term}

$$\sum_{d=1}^{n_f}\ [\Phi\ \ D_{wd}\ \ \rho_w\ \ \triangle\, w_{id}\ \ +\ \ \Phi\ \ D_{gd}\ \ \rho_g\ \ \triangle\, y_{id}\ \ +\ \Phi\ \ D_{od}\ \ \rho_o\ \ \triangle\, o_{id}]$$

{Dispersion Flow Terms in aqueous, gaseous and oil phases}

$$\partial_{iw}\sum_{d=1}^{n_f}[\ (\rho_w\, q_{wk}\, w_i)\ +\ \left(\rho_g\ \ q_{gk}\ \ y_i\right)\ + (\rho_o\ \ q_{ok}\ \ o_i)\ \ ]\ ,\ldots\ldots\ldots\ldots(17)$$

{Source / Sink Terms for aqueous, gaseous and oil phases}

where w, g and o conventions represent aqueous, gaseous and oil phases respectively, '*d*' represents the flow between two neighboring grid block faces, 'n_f' represents the total number of neighboring grid blocks; T_w, T_g and T_o represent the phase transmissibilities in aqueous, gaseous and oil phases; $\triangle \phi_w$, $\triangle \phi_g$ and $\triangle \phi_o$ represent the potentials faced by each phase; w_i, y_i and o_i represent the water, gas and oil phase concentrations of species 'i' respectively; $\triangle w_{id}$, $\triangle y_{id}$ and $\triangle o_{id}$ represent the differences in water, gas and oil phase concentrations between the nodes for species 'i' respectively, s'_{ki} represents the stochiometric coefficient of the reaction's product 'i' in reaction 'k'; s_{ki} represents the stoichiometric coefficient of the reaction's reactant 'i' in reaction 'k'; r_k is the reaction rate for reaction 'k'; D_{wi}, D_{gi} and D_{oi} are the effective dispersibilities, comprising the diffusion and mechanical dispersion coefficients of species 'i' in the aqueous, gaseous and oil phases, respectively; q_{wk}, q_{gk} and q_{ok} are the source/sink rates for aqueous, gaseous and oil phases in well layer *k*, respectively, and n_r is the total number of chemical reactions. 'n_r' equals two.

$$\frac{\partial}{\partial t}[V_v C_{calcite}] = V \sum_{k=1}^{n_r} (s'_{ki} - s_{ki})\ r_k\ , \quad \text{……………………………………………………...(18)}$$

where V_v is the void volume representation in ft^3, $C_{calcite}$ is the solid calcite mineral concentration in $lbmol/ft^3$.

$$\frac{\partial}{\partial t}[V_v C_{dolomite}] = V \sum_{k=1}^{n_r} (s'_{ki} - s_{ki})\ r_k\ , \quad \text{……………………………………….………...…(19)}$$

where $C_{dolomite}$ is the solid dolomite mineral concentration in $lbmol/ft^3$.

$$T_j = T\left(\frac{k_{rj}}{\mu_j}\right);\ j=w,g,o;\ \ T = k_{abs\_eff}\ \ A_{eff} / l_{eff}\ , \quad \text{…………………….......................……………….(20)}$$

where k_{rj} is the relative permeability to phase 'j'; μ_j is the dynamic viscosity of phase 'j'; k_{abs_eff} is the weighted harmonic average absolute permeability of the two grid cell regions, A_{eff} is the weighted harmonic average cross-sectional area of the two grid cells involved in the direction of fluid flow, and l_{eff} represents the weighted harmonic average node to node distance between grid cells.

The structure-property relations used toward the model's initialization, and to simulate dynamic variations in permeabilities with that of the porosities, during the carbonate mineral dissolution process, are given in below equations.

The diffusion equation for species ‘i’ in phase ‘j’ and direction ‘k’ is given by Eq. 21 (CMG STARS 2017).

$$J_{ijk} = -\left(\Phi\ S_j\ \frac{D_{ij}^{*}}{F_{jk}}\right)\ \boldsymbol{\nabla}_k\ (\rho_j\ \ x_{i,j}),\ \ldots\ldots\ldots\ldots\ldots\ldots\ldots\ldots\ldots\ldots\ldots\ldots\ldots\ldots\ldots\ldots(21)$$

where, D_{ij}^{*} is the molecular diffusion coefficient of component ‘i’ in phase ‘j', F_{jk} is the tortuosity factor for phase ‘j’ in direction ‘k’, and $\boldsymbol{\nabla}_k(\rho_j\ \ x_{i,j})$ is the concentration gradient of component ‘i’ in phase ‘j’ in direction ‘k’.

The dispersion equation for species ‘i’ in phase ‘j’ and direction ‘k’ is given by Eq. 22 (CMG STARS 2017).

$$J_{ijk} = -\left(\Phi\ \ S_j\ \alpha_{jk}\ |u_j|\right)\ \ \boldsymbol{\nabla}_k\ (\rho_j\ \ x_{i,j})\ ,\ \ldots\ldots\ldots\ldots\ldots\ldots\ldots\ldots\ldots\ldots\ldots\ldots\ldots\ldots(22)$$

where, α_{jk} is the mechanical dispersivity for phase ‘j’ in direction ‘k', and $|u_j|$ represents the magnitude of the interstitial velocity of phase ‘j’.

Oil-water and gas-liquid relative permeability curves have been defined using Corey's correlations, (Corey, 1954). The base permeability for this study is defined as the absolute permeability of the rock to water. The degree of rock wettability toward oil and water phases can be characterized by the shapes of the K_r curves. Based on Corey's correlations, the Corey exponents govern the shape of the curves, with a higher exponent value for a specific phase inducing a greater curvature, thus indicating a greater tendency of that phase to wet the rock.

Physically, a water-wet rock would mean that the water phase is on the rock surface, and the oil and gas phases occupy majority of the central pore space. The motion of water on a comparative note is restricted due to contact with and subsequent retention by the rock surfaces. The same would apply accordingly for an oil-wet rock. This implies that in a water-wet system, the third phase, i.e., gas in the pores, if any, would compete with the non-wetting oil phase. Mathematically, this mechanism is formulated in the numerical model by a three-phase relative permeability formulation, as stated below.

k_r inputs for oil-water and gas-oil interactions are manually defined. The three-phase calculation is given by Equation 23 (CMG STARS 2017).

$$k_{ro} = k_{rocw}\,((k_{row}/k_{rocw} + k_{rw})\,(k_{rog}/k_{rocw} + k_{rg}) - k_{rw} - k_{rg}) \ldots\ldots\ldots\ldots(23)$$

where k_{ro} is the k_r to the oil phase; k_{rocw} is the k_r to the oil phase at initial water conditions; k_{row} is the k_r to the oil phase in the presence of water in the water-wet medium; k_{rw} is the k_r to the water phase in the water-wet medium; k_{rog} is the k_r to the oil phase in the presence of gas; k_{rg} is the k_r to the gas phase in the water-wet medium.

3.7 Model Limitations & Assumptions

The carbonate minerals are stationary in the pore space. Their concentration in a location changes only via consumption through the defined chemical reactions. All grid cells in the model are isothermal, at the defined laboratory temperature of 150°F. The capillary pressures were neglected in this study. HCl, $CaCl_2$ and $MgCl_2$ are in the aqueous phase at all times. The dispersion magnitudes of all components defined in the aqueous phase are similar. The chemical reactions were limited to the aqueous-mineral interactions, and the individual homogeneous aqueous reactions were beyond the scope of this study.

The evolved CO_2 from the HCl-Calcite chemical reaction is designated in such a manner that 50% is aqueous-phase soluble (CO_2-w), and the other 50% is oil-phase soluble (CO_2-o). For given local pressure, temperature and salinity conditions, any un-dissolved CO_2 fractions remain as a gaseous/liquid/supercritical phase, but take up relative permeability values similar to the corresponding parent phase. Thus, if the insoluble CO_2 exists at liquid / supercritical conditions, the CO_2-o fraction will adopt relative permeability values similar to that of the oil-phase, and CO_2-w fraction will adopt relative permeability values similar to that of the aqueous-phase. Likewise, if the insoluble CO_2 exists as a gas, both CO_2-o and CO_2-w fractions will adopt relative permeability values similar to that of the gaseous-phase.

3.8 Crude Oil Characterization

The composition primarily consisted of semi-light hydrocarbon fractions between C6 and C15. The 41 °API oil, as measured experimentally, was in the light oil window. At test temperatures of 150°F and pressures at and above 14.7 psi, the fluid model predicted the oil to be completely in the liquid phase window. A numerical simulation of CO_2-crude oil swelling test was performed, in which, the soluble CO_2 in crude oil was said to swell the oil up to 1.65 times its original volume at 1,200 psi pore pressures, provided an enough supply of CO_2 exists. An analytical tie line approach was used toward estimating the minimum miscibility pressure of CO_2 in the crude oil system, and the onset of miscibility was estimated at 1,600 psi onwards.

The developed fluid model by Kumar et al. (2020) was modified toward the purpose of this study. A lumping scheme was performed based on a combination of similar ranges in critical points of components and their mole fractions, to reduce the total number of components to 4 lumped groups, namely IC4-NC5; FC6-FC14; FC15-FC20; FC21-FC38. CO_2-o was included as the fifth component, initially stated to be present in the crude oil in negligible fractions. The lumped crude oil model mimicked the experimentally measured viscosities and densities of the crude oil, with respect to temperature, to a good level of accuracy. The measured density and viscosity of the crude oil at 150°F and 14.7 psi were 48 lb/ft^3 and 1.5 cp respectively.

4. COREFLOOD AND MODELING RESULTS*

Four pre-flush sandstone acidizing experiments were conducted on cores I, II, III and IV, with the saturations of I and II being at S_w=1, III at $\mathbf{S_{wi}}$, and IV at $\mathbf{S_{orw}}$. All pre-flush experiments were conducted horizontally, at 1,200 psi initial pore pressures, 2,000 psi overburden pressures, and temperatures of 150°F.

The cases for cores II and IV were selected toward modeling studies. The model's grid cell dimensions were set as dI = 0.067 cm, dJ & dK = 0.1524 cm, to mimic the core's physical measurements. Both cores were CT scanned in their dry and water saturated states, in order to determine the porosity distribution, as per the method by Akin and Kovscek (2003). The original image resolution of the CT scanner for the cores were 534 x 512 x 512 pixels, in the I x J x K coordinates. A level of comprise was struck upon reduction in the resolution to a 152 x 25 x 25 system, in order to suit the grid configuration of the numerical model, by averaging with a bilinear interpolation technique.

The populated permeabilities and porosities were calibrated initially with the absolute permeability experiments performed on the cores. The fluid saturations representative of the core

---

* Part of this chapter is reprinted with permission from "A Three-Phase Study on Pre-Flush Stage in Sandstone Acidizing: Experimental and Modeling Analysis of Evolved CO_2 in a Hydrocarbon and Aqueous Environment" by S. Muhemmed, H.T. Kumar and H.A. Nasr-El-Din, 2019. 2019 SPE Annual Technical Conference and Exhibition, SPE-195897-MS, Copyright 2019 by SPE.

being modeled was defined. The composition of aqueous phase injection fluids defined in the simulation cases were as per the required acid concentrations.

The quantities used in history matching the model with the pre-flush experimental data were the corefloods' effluent concentrations and volumes. The collected effluents were used toward measuring the concentrations of $MgCl_2$ and $CaCl_2$, which are reaction products from the dolomite and calcite mineral dissolution processes, through an inductively coupled plasma optical emission spectrometry (ICP-OES). Fig. 7 provides step wise procedures that were followed in the history matching process.

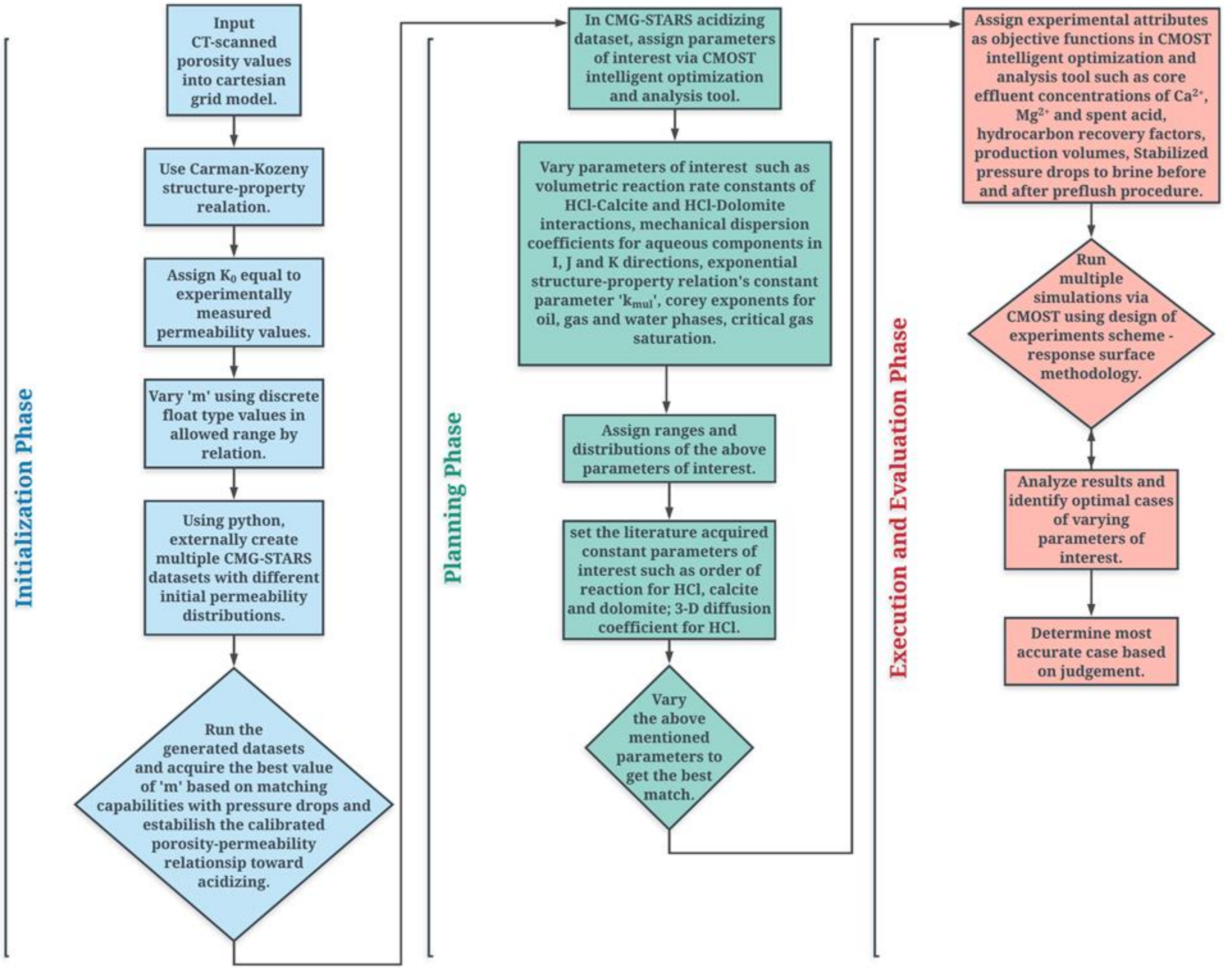

Fig. 7—History matching procedures of numerical model with experimental results, as followed in the preflush acidizing simulation datasets.

4.1 Fully Water Saturated Cores

Cores I and II were of 100% S_w. The purpose of acidizing brine saturated cores was to judge the efficiency of carbonate dissolution, as well as quantify the amount of CO_2 being produced.

Core I was initially injected with 10 wt% KCl at 3 cm^3/min, until a stabilized pressure drop was achieved. After this, the injection was switched to 15 wt% HCl at the same flow rate. As the acid reacted with the carbonate minerals, a sharp increase was observed in the pressure drops across the core, as can be seen in Fig. 8.

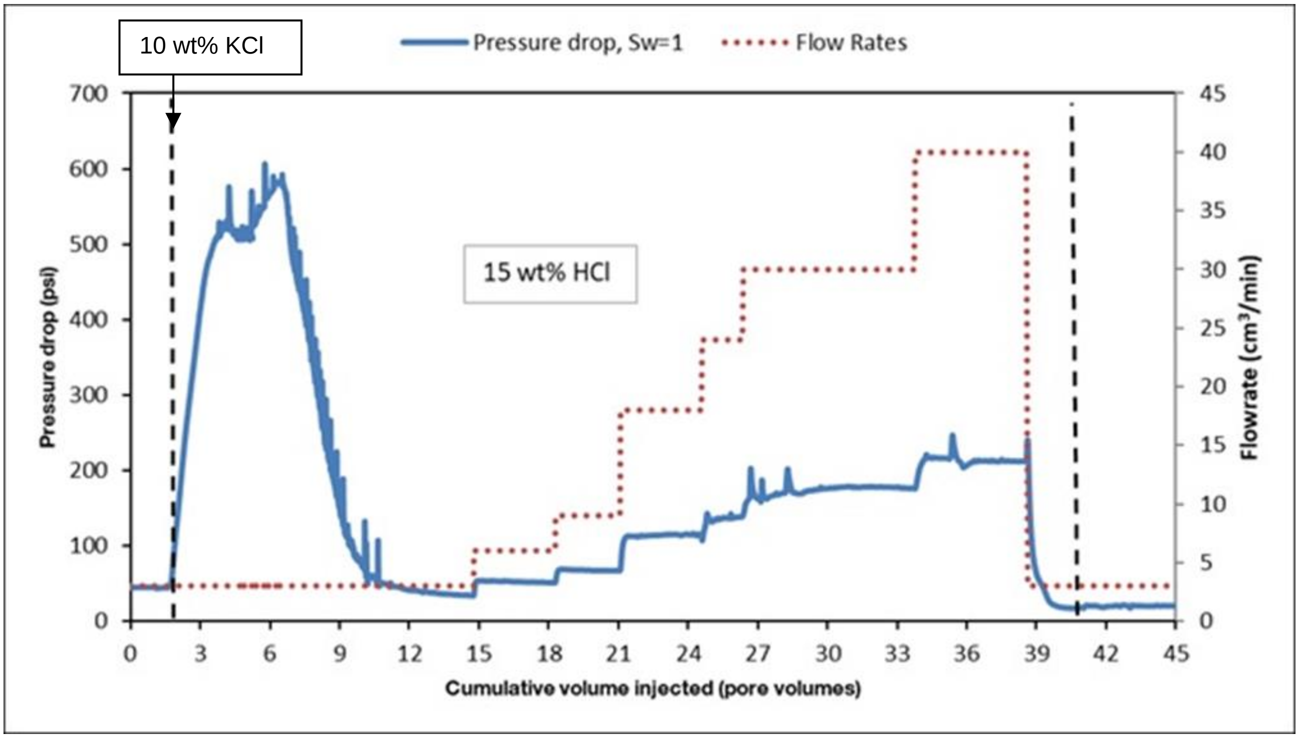

Fig. 8—Pressure drop and injection rates as a function of the cumulative volume of injected fluids, for core I, 100% brine saturated case.

This increment is associated with the generation of the chemical reaction products during the HCl - carbonate minerals' interaction, namely, H_2O, CO_2, $CaCl_2$ and $MgCl_2$. Table 8 provides the extent of CO_2's solubility in brine at pore pressure and temperature conditions, as well as the extent of changes in the aqueous phase viscosities. A very minor fraction of CO_2 is soluble in the aqueous phase at the existing conditions, with a maximum possibility of 1.61% in mole fractions, and thus has a minimal influence on aqueous phase viscosities and densities.

Table 8—Parameters used in the numerical model to accurately mimic the pre-flush experiment performed on core II, fully water saturated case, listed in the order of influence.

History Matching Parameters for Core II's Pre-flush Experiment	
HCl concentration reaction order	1
Calcite concentration reaction order	0
Dolomite concentration reaction order	0
Diffusion coefficient (3D), cm^2/s (after Fredd and Fogler 1999)	3.59×10^{-5}
History-Matched Parameters	
Volumetric reaction rate constant (Calcite + HCl), s^{-1}	1.16
Volumetric reaction rate constant (Dolomite + HCl), s^{-1}	0.12
Mechanical dispersion coefficient (I direction), cm	0.000684
Mechanical dispersion coefficient (J, K directions), cm	0
Porosity-permeability exponential relation constant, k_{mul} (I direction)	12
Porosity-permeability exponential relation constant, k_{mul} (J, K directions)	12
Water Corey exponent, N_w	2.5
Gas Corey exponent, N_g	2.5
Critical gas saturation	0

The remaining of the evolved CO_2 exists at supercritical conditions, during which CO_2 portrays viscosities of 0.02 cp. When one mole each of calcite and dolomite minerals react with HCl, the corresponding volumetric occupancy of the evolved CO_2 is approximately 680 cm^3 at the pore conditions. Amongst all the products, CO_2 being a compressible fluid tends to influence the pressure drops by a larger extent. **Fig. 9** shows a plot of the concentrations of $CaCl_2$ and $MgCl_2$ versus the PV's of acid injected.

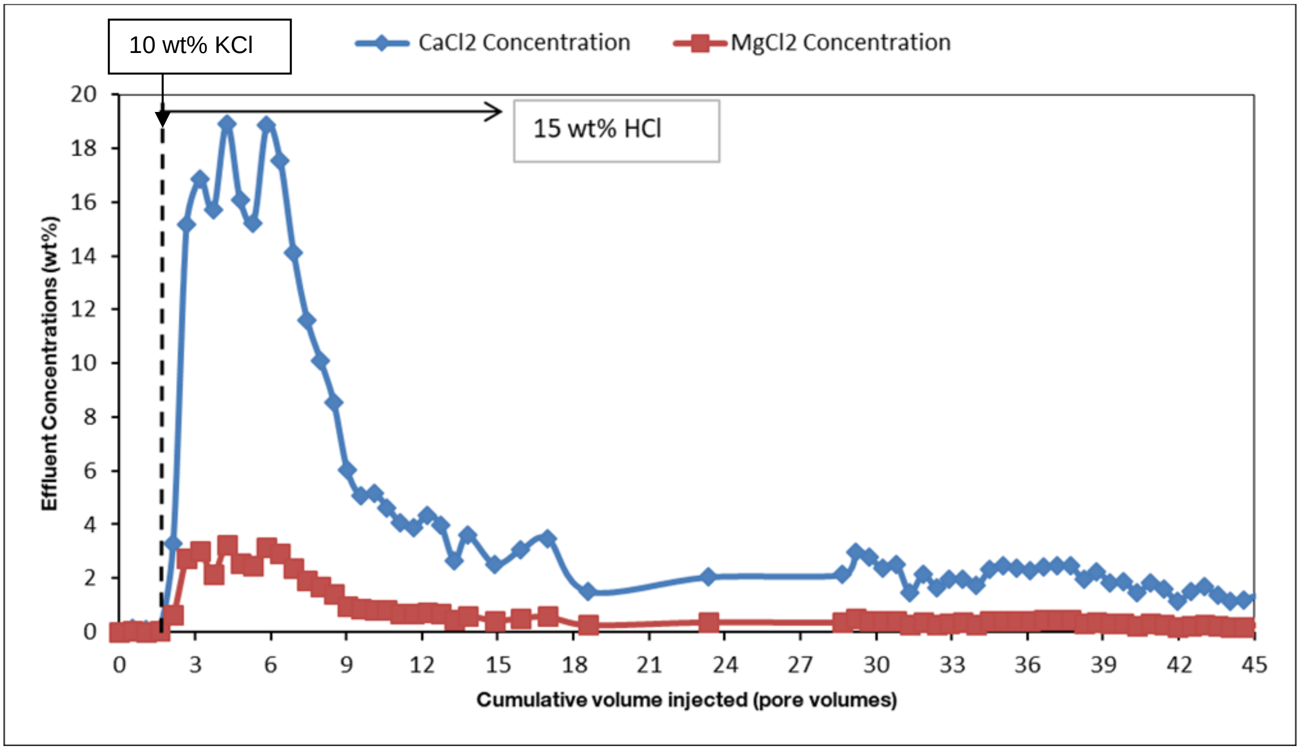

Fig. 9—Effluent concentration of $CaCl_2$ and $MgCl_2$ as a function of the cumulative volume injected fluids for core I, 100% brine saturated case

The concentration gradient of the $CaCl_2$ and $MgCl_2$ follow an almost similar trend as the pressure drop gradient curve in Fig. 8. Once the pressure drop curve stabilized for a 3 cm^3/min acid injection rate, the rates were increased in steps. The incremental flow rates were 6, 9, 18, 24, 30 and 40 cm^3/min, with between 2 to 6 PV's of injection per flow rate, as also seen in Fig. 7. After this, the flow was switched to brine injection at 3 cm^3/min, to remove any acid from the core. As can be seen in Fig. 8, there is always a finite amount of $CaCl_2$ and $MgCl_2$ being produced, upon increasing the flow rates. At the initial rate of 3 cm^3/min, the permeability in the regions of carbonate dissolution increases, creating regions of paths of least resistance within the core. This results in a preferential flow path for the fresh incoming acid, leading to selective and non-uniform carbonate mineral dissolution across the core. Increasing flow rates help divert the fresh acid to regions which were not swept by the acid previously, thus dissolving more carbonate minerals across the core. Based on the measured effluent concentrations, a total of 34.2 g of calcite and 15.4 g of dolomite was calculated to be dissolved. This dissolution generated a calculated equivalent of 11.4 liters of CO_2 at standard temperature and pressure (STP) conditions. **Fig. 10** shows core I after the pre-flush stage. The presence of a tan shade on the outer periphery of the core signifies the presence of carbonate minerals. Few drops of 15 wt% acid on the tan shaded region created a brisk effervescence, hence validating the presence of **untouched carbonate minerals**. Even after injecting around 40 PV's of acid at the above-mentioned rates, complete dissolution of carbonate minerals was not achieved. A large portion of the core remained untouched. This is attributed to the rock heterogeneity, and the nature of the fluid to flow in the path of least resistance that is created during the dissolution process.

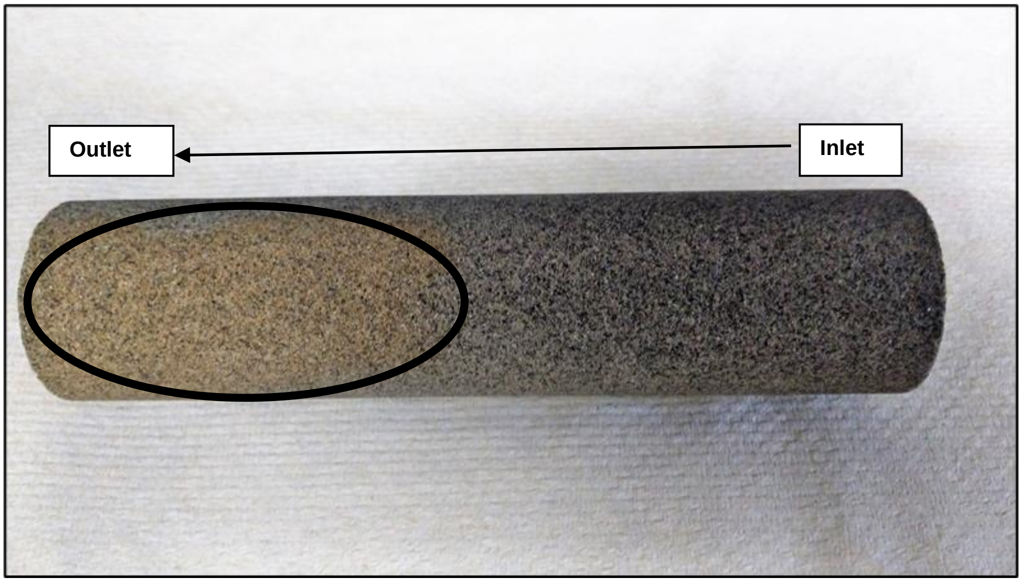

Fig. 10—Carbon Tan core 1 after injecting 15 wt% HCl at multiple flow rates, with the circled tan shade implying unreacted carbonate minerals.

Likewise, in the field, pumping a select volume of pre-flush will not guarantee the eradication of all carbonate minerals from the damaged zone, thus posing the possibility of severe precipitation during the main-treatment.

Furthermore, from the conducted XRD results, it can be inferred that carbonate minerals constituted 11.2 wt% of the total rock mineralogy. The total amount of carbonate minerals dissolved through acidizing was 49.6 g, which is equivalent to 12.3 wt% of the core. Thus, the XRD method may not be a completely accurate representative technique to estimate mineralogy distribution across the sandstone cores.

For Core II, the injection rate was set at 1 cm^3/min, keeping all other conditions similar to that followed for core I. The pressure drop curve and the concentration of $CaCl_2$ and $MgCl_2$ are shown in **Figs. 11 and 12**.

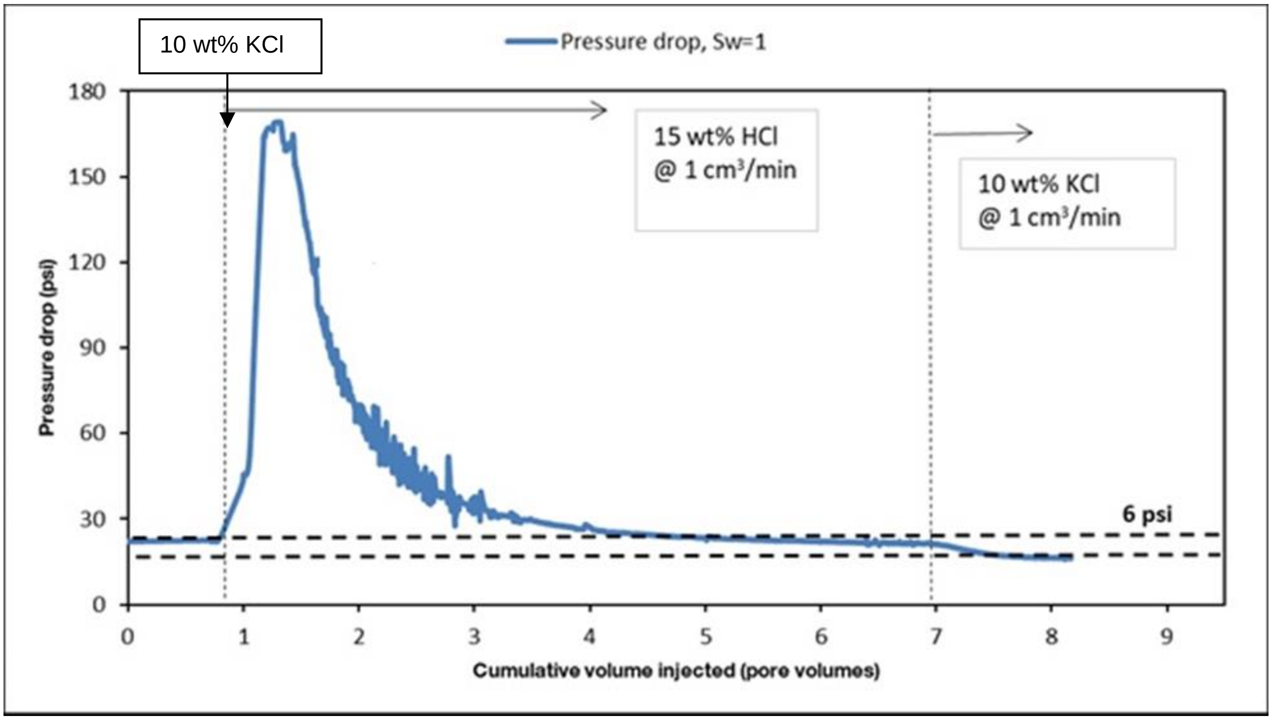

Fig. 11—Pressure drop as a function of the cumulative volume of injected fluids for 100% brine saturated core, core II, at 1 cm^3/min injection rate.

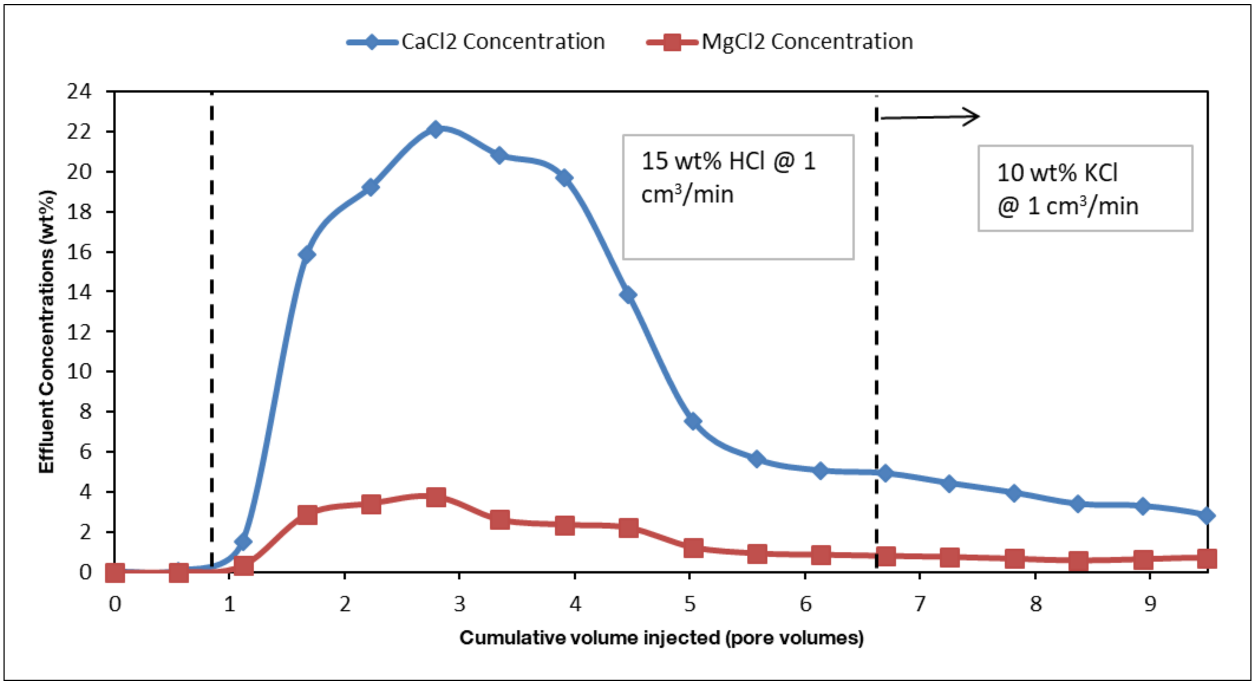

Fig. 12—Effluent concentration of $CaCl_2$ and $MgCl_2$ as a function of the cumulative volume of injected fluids for 100% brine saturated core, core II, at 1 cm^3/min injection rate.

The acid injection continued until the pressure drop curve stabilized, indicating no further CO_2 evolution, and thus no more carbonate dissolution in the core. As expected, at 1 cm^3/min, there was an even lower dissolution of carbonate minerals in core II, as is evident from the tan shaded regions shown in **Fig. 13.** After the acid injection, the flow was switched to brine while maintaining the same flow rate, to remove any acid in the core. The pressure gradient to brine, post-acid injection, stabilized at a value 6 psi lesser than that of brine prior to acid injection, for the same flow rate of 1 cm^3/min. This shows a direct improvement in permeability across the core, due to carbonate mineral dissolution. A total of 7 PV's of the acid was injected at 1 cm^3/min, and the effluent concentrations were analyzed, yielding 23.5 g of carbonate minerals being dissolved. This generated an equivalent calculated CO_2 volume of 5.4 liters being produced at STP conditions. As expected, the presence of tan shades across core II, indicating the un-reacted regions, is significantly higher than that shown in core I.

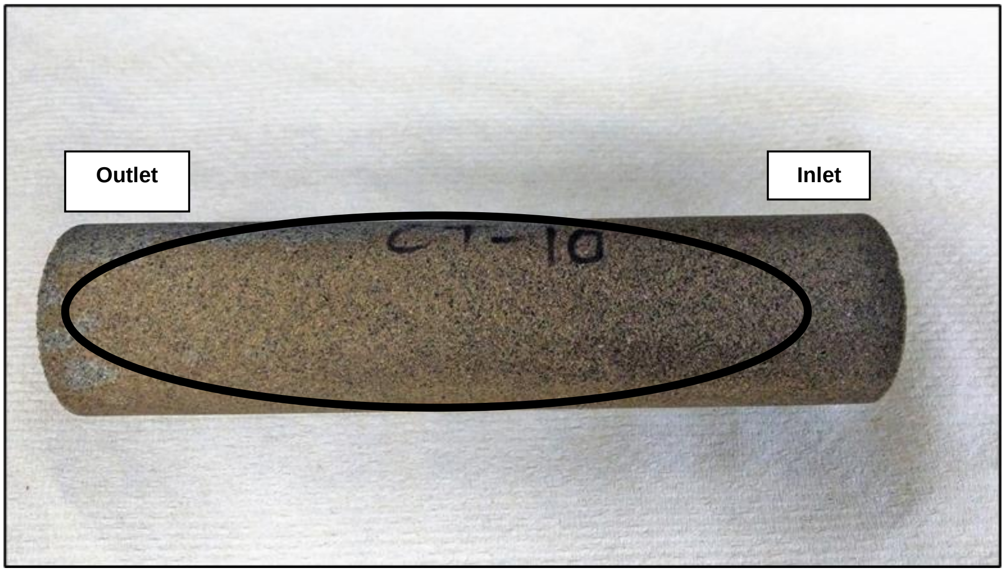

Fig. 13—Carbon Tan core II after injecting 15 wt% HCl at 1 cm^3/min, with a high tan shade implying unreacted regions.

The core II case was simulated using the numerical model, with similar experimental controls. **Fig. 14** shows the core model representation, with the CT scan based porosities populated across the model. Upon analyzing Figs. 13 and 14 together, the layers in the top of the model in Fig. 14 show low porous zones, indicating low permeabilities. Thus, the acid may not have easily penetrated these regions due to high resistance, resulting in the tan shade in the top layers of Core II (Fig. 13). **Fig. 15** depicts the history match of the simulation with that of the experiment, for the effluents' $CaCl_2$ and $MgCl_2$ concentrations.

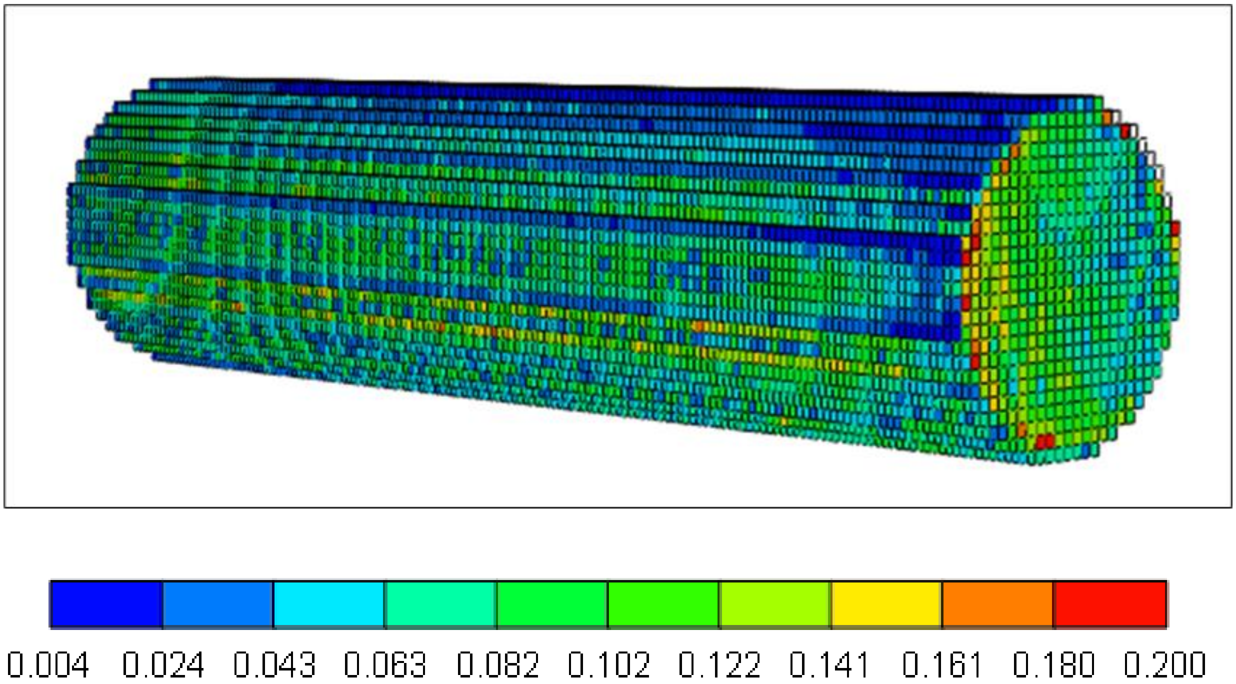

Fig. 13—Core model showing the representative CT scan mapped initial porosity distribution across the core II.

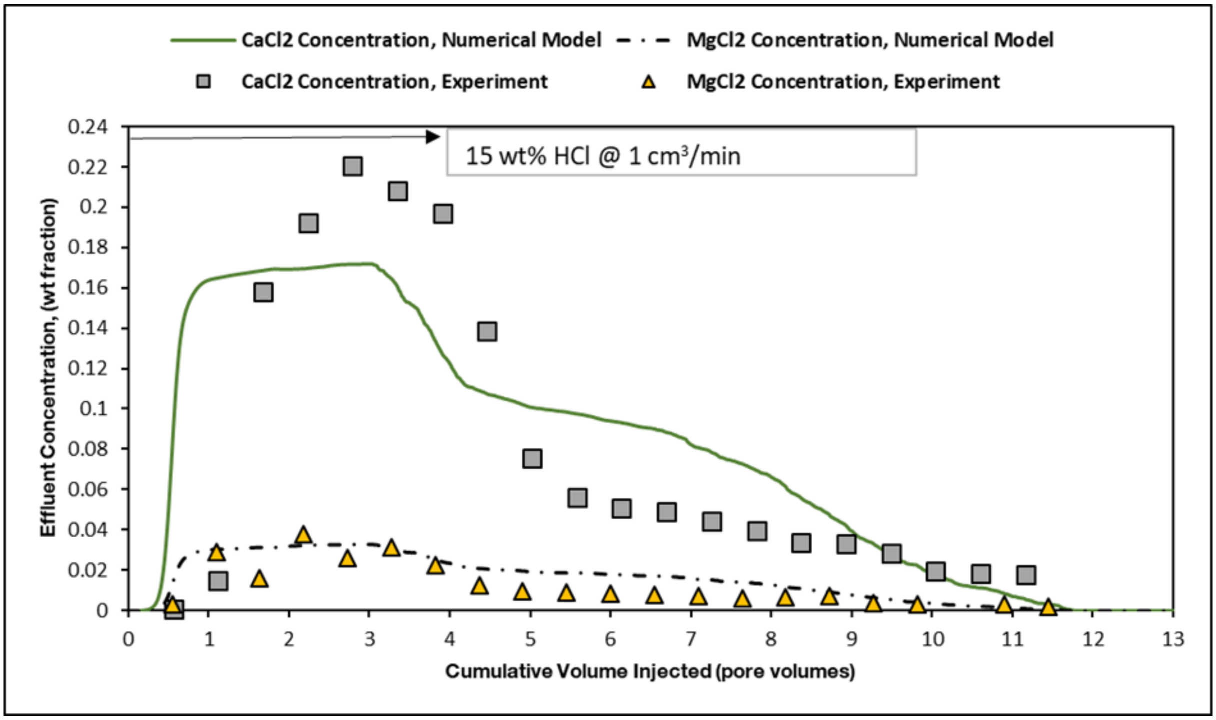

Fig. 15—Effluent concentration of $CaCl_2$ and $MgCl_2$ matched between model and experimental values at 150°F, for core II's case.

The model matches most of the experimental points, and maintains the same trend in behavior. The offsets in match is attributed to the uncertainty in initial mineralogy distribution in the core. **Table 8** gives the history matching parameters for the best match scenario obtained, listed in the order of influence. The diffusion coefficient of HCl was taken from Fredd and Fogler (1999). **Fig. 16** shows a plot as output from the simulation run, representing the cumulative CO_2 production curve for the simulated period. The trend in slopes of the CO_2 cumulative production curve is directly proportional to the magnitude of total concentrations of the carbonate mineral dissolution products as observed in the effluents.

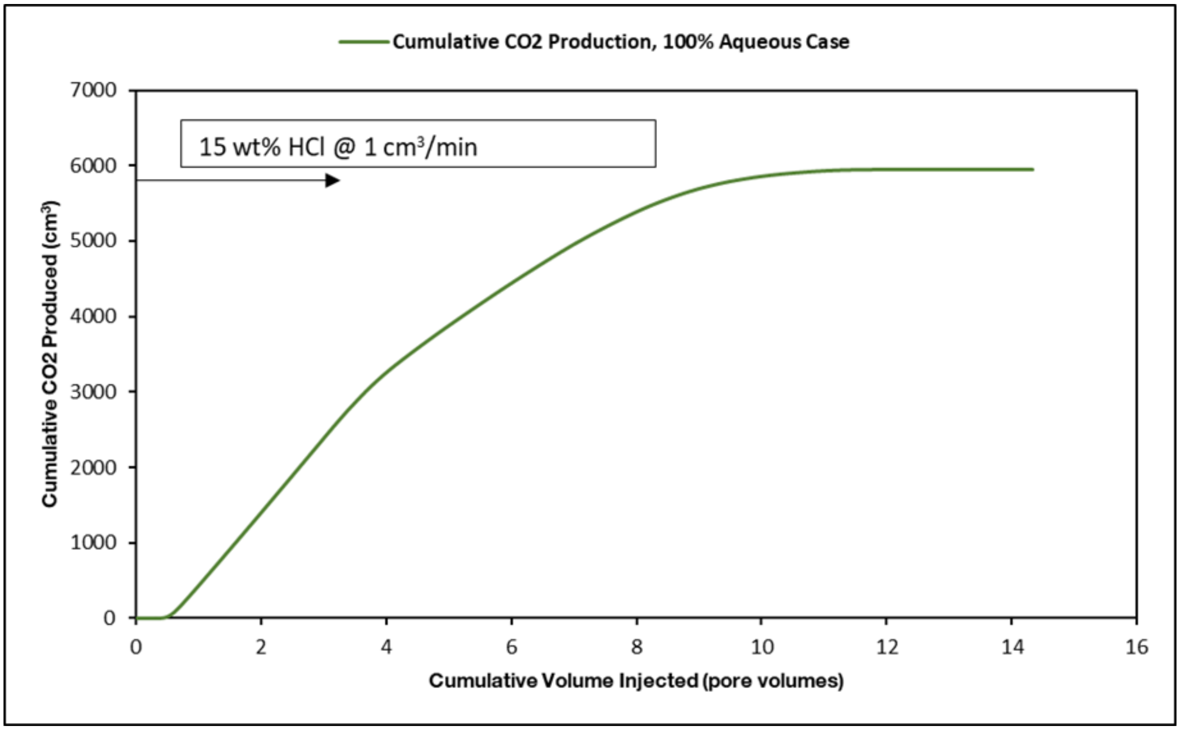

Fig. 16—Cumulative CO_2 produced as a function of the cumulative volume of acid injected in the modeled core, for core II's case.

The total cumulative CO_2 production of 5.85 liters at STP conditions, as predicted by the model is close to that of the experimentally calculated value of 5.4 liters. Therefore, the numerical model is capable of predicting the experimental results, for the 100% aqueous cases, to a good level in accuracy.

4.2 Core with Initial Water Saturation

The initial water saturation in Core III, constituted 39% of the pore space**.** Keeping all experimental conditions similar to the pre-flush experiments described in cores I and II, the crude oil was initially injected at 1 cm^3/min until a stabilized pressure drop was achieved. After this, the flow was switched to acid at the same rate. Similar to earlier observations, the production of CO_2 due to calcite and dolomite dissolution causes a sharp increase in the pressure gradient across the core, as shown in **Fig. 17**. **Fig. 18** shows the measured effluent concentrations of $MgCl_2$ and $CaCl_2$, which were used toward calculation of total minerals dissolved in the core.

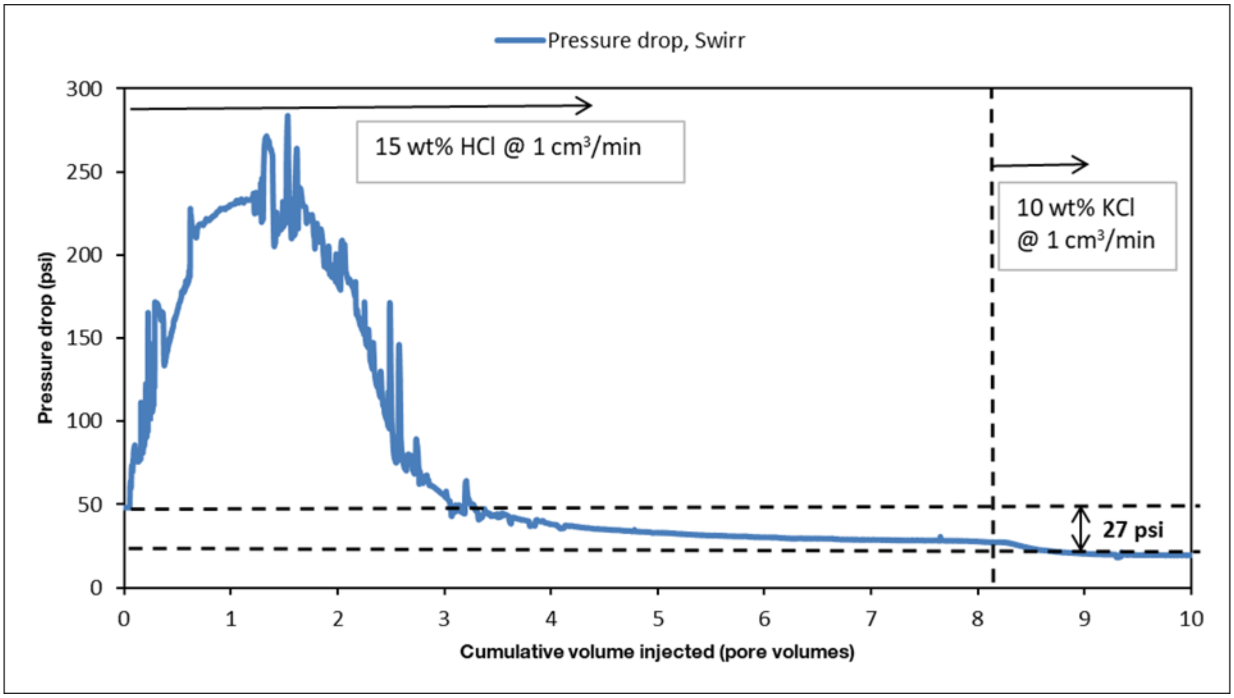

Fig. 17—Pressure drop as a function of the cumulative volume of injected fluids for oil saturated core, core III.

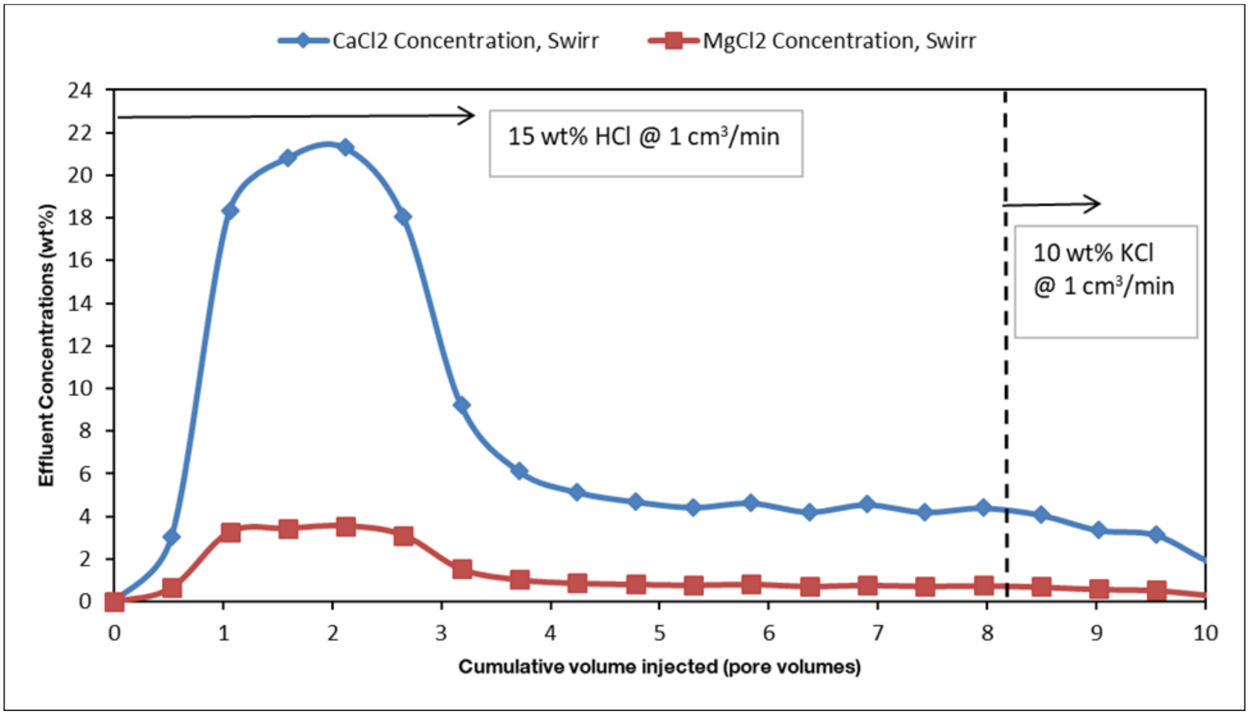

Fig. 18—Effluent concentration of $CaCl_2$ and $MgCl_2$ as a function of the cumulative volume of injected fluids for the oil saturated core, core III, at 1 cm^3/min injection rate.

After injecting 8 PV's of acid, the flow was switched back to brine at the same rate. A total of 22.6 g of carbonate minerals was calculated to be dissolved, which generated a calculated equivalent of 5.2 liters of CO_2 at STP conditions. Of the 13.8 cm^3 of oil initially present in the core, a total of 8.9 cm^3 of oil was produced, yielding a 64.5% oil recovery. This value was 10.5% higher than the oil recovery achieved in core IV from waterflooding (**Table 2**). Given the fact that both cores were of similar rock type and properties, the overall oil production in core III was attributed to two mechanisms - a) waterflooding, and b) CO_2 assisted mobility of crude oil. The additional 10.5% oil recovery from core III, in comparison to core IV, is attributed to the latter. More detail on the CO_2 related mechanisms is given in the following sections.

4.3 Core with Residual Oil Saturation to Waterfloods

The initial oil saturation in Core IV, constituted 29% of the pore space, i.e., 6.4 cc at residual conditions. Keeping all conditions similar as in the previous pre-flush experiments, brine was initially injected at 1 cm^3/min into core IV. When a stabilized pressure drop was achieved, the flow was switched to acid. **Figs. 19 and 20** show the pressure gradient and the concentrations of $CaCl_2$ and $MgCl_2$, as a function of PV's of fluids injected.

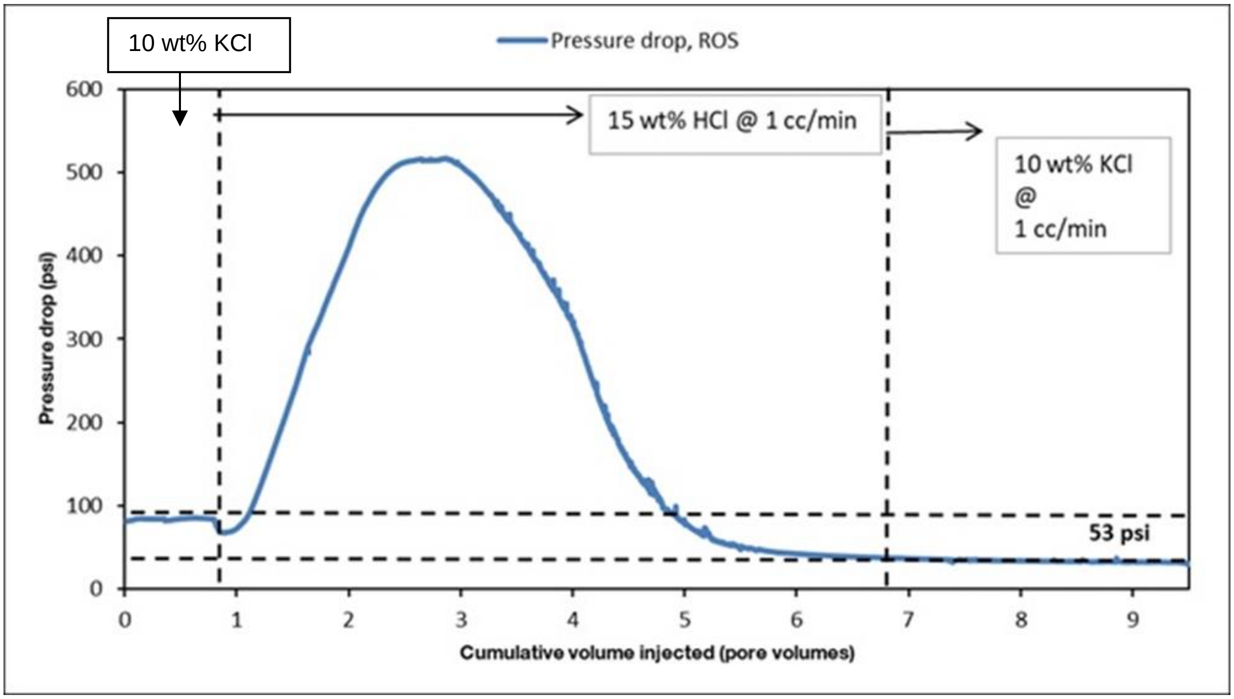

Fig. 19—Pressure drop as a function of the cumulative volume of injected fluids for the core IV at residual oil conditions, performed at 1 cm^3/min injection rate.

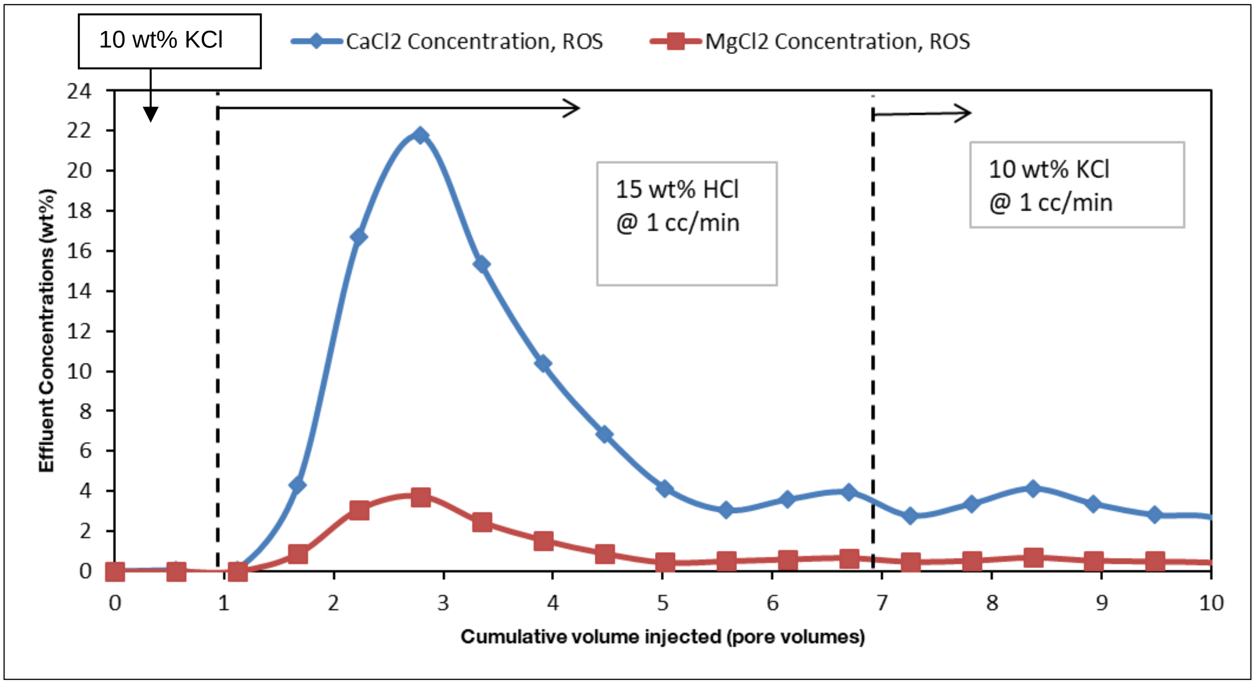

Fig. 20—Effluent concentration of $CaCl_2$ and $MgCl_2$ as a function of the cumulative volume of injected fluids, for core IV at residual oil saturation conditions, performed at 1 cm^3/min injection rate.

A total of 16.5 g of carbonate minerals were calculated to be dissolved, producing an equivalent calculated 3.8 liters of CO_2 gas at STP conditions. During the acidizing stage, 1.6 cm^3 of oil was recovered, which is equivalent to 25.6% of residual oil initially in place. The effective permeability to water, K_{ew}, at $\mathbf{S_{orw}}$ for core IV increased from 5 to 14 md, due to carbonate minerals' dissolution.

The numerical model was used to simulate and match the pre-flush experiment conducted on the core IV with oil at residual conditions. The model was initialized with the lumped crude oil at residual conditions, and using uniform pore pressures of 1,200 psi and temperatures of 150°F. All control parameters were similar as used in the experimental counterpart. The chemical reaction parameters were adopted from the experimentally history matched fully water saturated core case, and other history matching parameters were maintained the same. The relative permeability formulations were set at water-wet conditions for the sandstone core model, with all the end points obtained from experiments. The Corey oil exponent, N_o, used to history match the experimental attributes was 2.5.

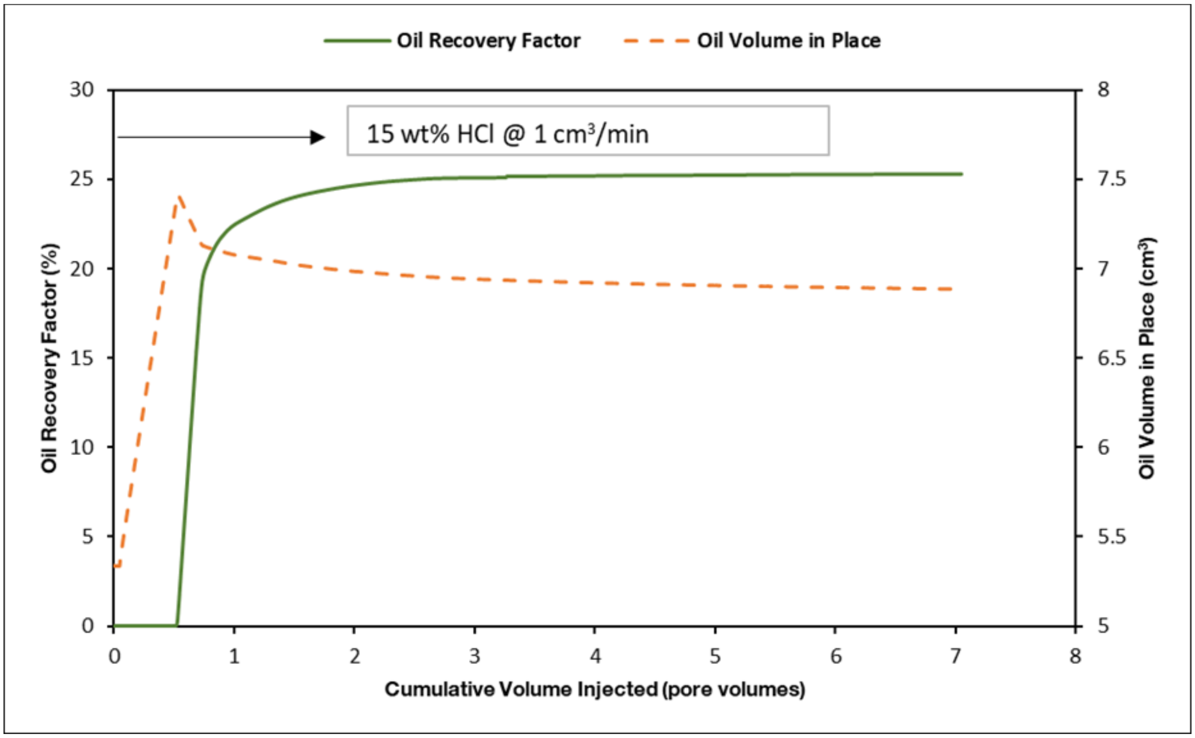

Fig. 21—Oil recovery as a result of evolved CO_2, as a function of the cumulative pore volumes of acid injected in the modeled core, for core IV's case at residual oil saturation conditions.

Fig. 21 shows the oil recovery factor and dynamic oil volumes in place, during the acid injection stage. As can be seen, 7 PV's of acid injection was simulated, similar to that of the experiments, and up to 25.3% of the residual oil in place was recovered from the damage zone. The oil volumes are shown to rise from 5.2 to 7.5 cc initially, at about 0.5 PV of acid injection, and no oil was seen to be produced at this period. After this point of 0.5 PV acid injection, the oil volume in place starts to reduce, and oil production is observed. As acid reacts with the carbonate minerals, the generated CO_2 is soluble in the oil phase. This solubility of CO_2 in oil causes a temporary increase in oil volume in place, and is known as the swelling mechanism. As mentioned earlier, the oil has the capability to swell up to 1.65 times its original volume, at pressures of 1,200 psi, provided a sufficient amount of CO_2 is supplied. However, during this increase in oil volume, we see no oil production, until after a particular point. This is explained by the residual end point saturation value for oil. As oil volume slowly increases, the oil saturation in place increases, and this shifts the value from $\mathbf{S_{orw}}$ to a higher magnitude, thus enabling the oil to now be mobilized by the incoming aqueous phase. The final oil recovery factor of 25.3% from the damaged zone, as predicted by the model, is similar to that observed in the performed coreflood test. Most of the oil is produced by 2 PV's of acid injection, a phenomenon which was also observed via the experiment. The oil produced from that point onwards is finite, and at extremely small rates. The extreme small rate of produced oil is from the contribution of CO_2, evolved from those pockets of carbonate minerals in the core inefficiently contacted by the incoming acid.

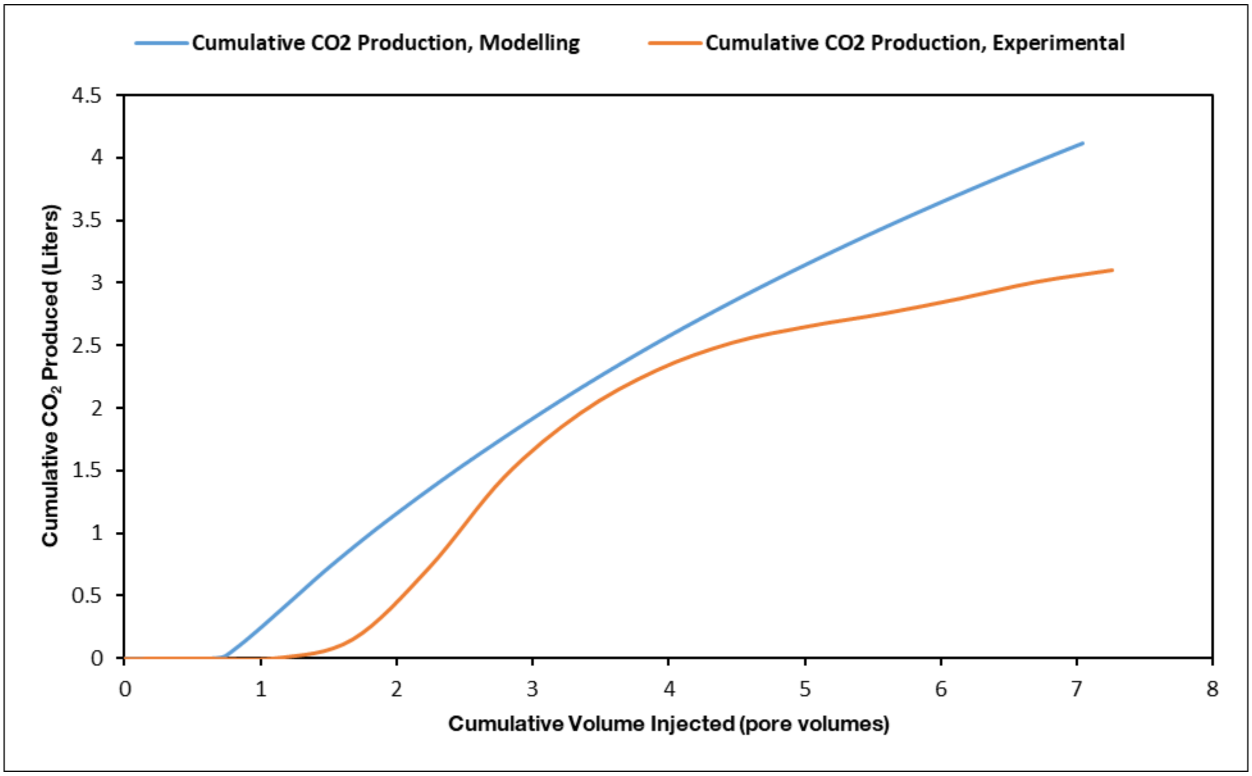

Fig. 22—Cumulative CO_2 produced as a function of the cumulative volume of acid injected for the simulated and experimental cases representative of core IV, at residual oil saturation conditions.

Fig. 22 shows the cumulative production of CO_2 produced between the numerical model, and that estimated from the experiment conducted on core IV, at STP conditions. As discussed earlier in fully water saturated cores, a major fraction of the carbonate minerals remains untouched, especially at low rates, and this applies to the core with initial residual oil saturation as well. **Figs. 23 and 24** show the CO_2 mole fraction in crude oil, and the crude oil saturation distributions respectively, for the simulated case at residual oil conditions, at the same layers and times.

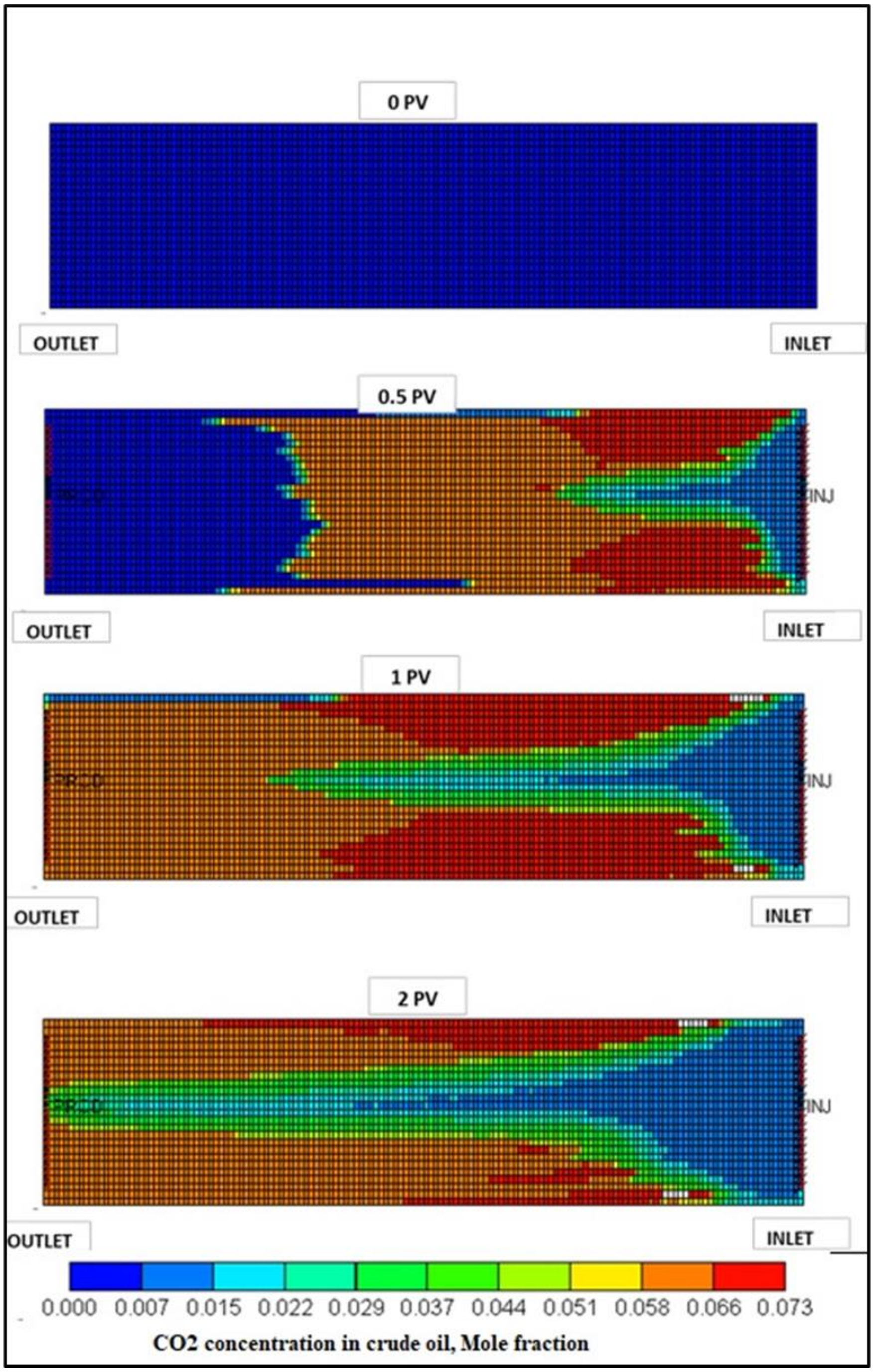

Fig. 23—Cross sectional view of middle layer of the core model as a function of acid pore volume injected and CO_2 saturation across the core, for core IV's case, in mole fraction.

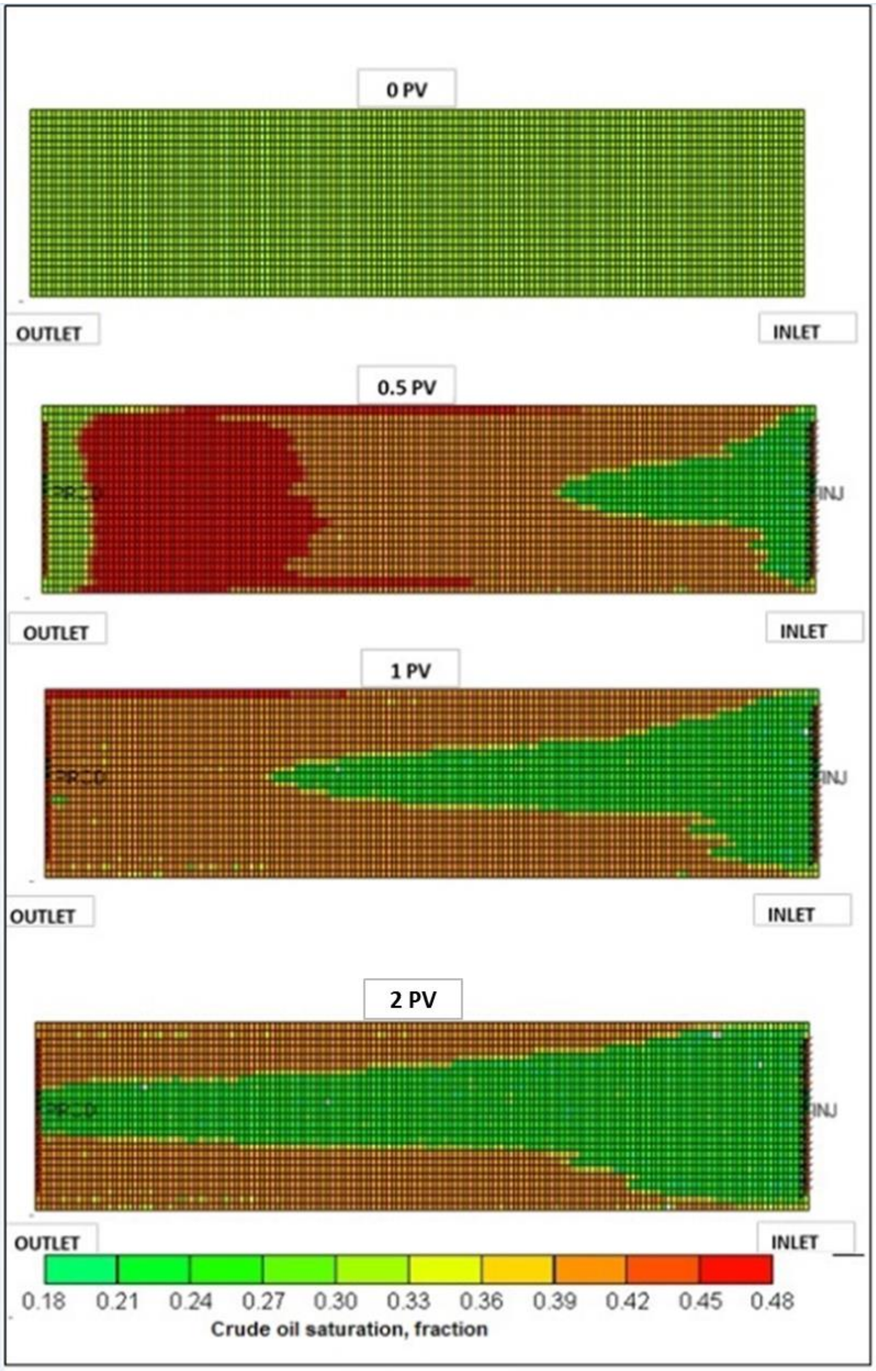

Fig. 24—Cross sectional views of the middle layer in the core model representing core IV's case.

The oil saturation distribution is shown as a function of acid pore volumes injected.

As can be seen, there is a direct correlation between the number of moles of CO_2 in crude oil, and that of the oil saturations. The CO_2 region is well ahead of the penetrating acid region and the evolved CO_2 will displace the oil by swelling the oil before the acid encounters oil. This proves that the CO_2 swells the oil in place, and thus increases the oil saturations. At 0.5 PV of acid injection, the CO_2 mole fraction map and corresponding oil saturation map show that the CO_2's reach in crude oil extends to 3/4th in length of the layer, and the oil in this region is swelled. In the remaining length of the core at this time, the CO_2 mole fraction in oil is zero, however, the oil saturation is around 0.48. This is because as the oil swells in volume, it dynamically reaches a non-residual saturation value capable of being swept by the incoming aqueous phase. Thus, oil is pushed toward the outlet face of the model. **Fig. 25** shows the calcite concentration distribution map for the same residual oil case, at similar layers and times. The sweep of the acid is non-uniform. As more porous pathways are created at the initial length, the incoming acid preferentially follows these paths of least resistance, and thus fail to sweep the other zones of carbonate minerals.

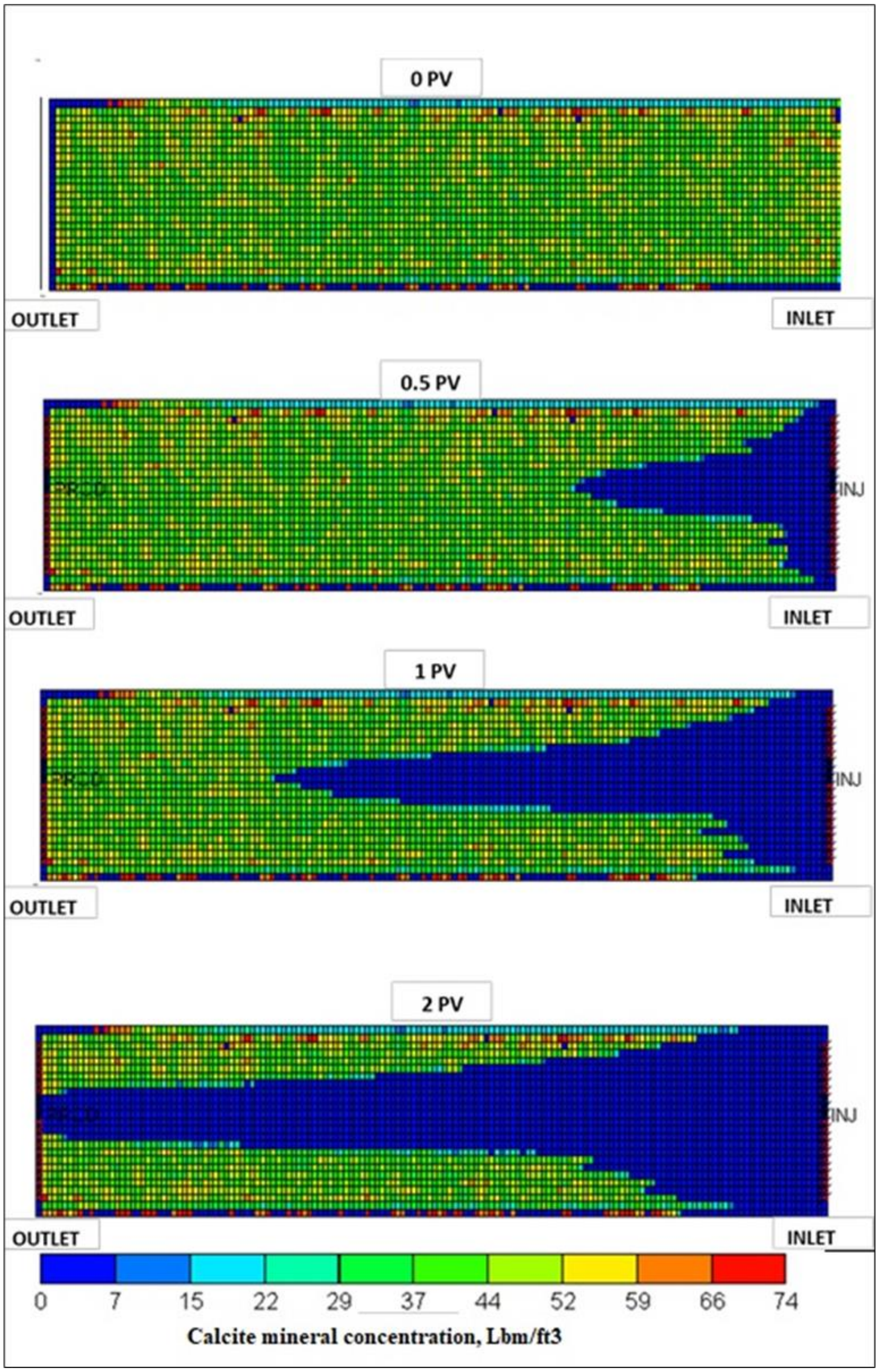

Fig. 25—Cross sectional view of middle layer the core model as a function of acid pore volumes injected and dissolved calcite concentration distribution, for the core IV's case in lbm/ft^3.

5. CONCLUSIONS AND RECOMMENDATIONS

5.1 Conclusions

A thorough analysis of sandstone acidizing pre-flush stages has been performed. A compositional three-phase perspective is undertaken, via experimental studies followed by numerical modeling. The important findings from the pre-flush analyses are mentioned below:

1. Incomplete carbonate mineral dissolution is achieved despite injection close to 40 pore volumes of 15 wt% HCl into the fully water saturated sandstone cores. Aside from the initial levels of heterogeneity, additional heterogeneity can be induced in the porous media during mineral dissolution, due to paths of least resistance to flow being created by the generated pore space. This results in preferential flow of the incoming acid, thus resulting in several regions of un-reacted carbonate minerals in the porous media.

2. During the pre-flush stage, the evolved CO_2 from carbonate mineral dissolution plays an important role in recovering fractions of the residual oil in place from the damaged zone, primarily via oil swelling mechanisms. CO_2 solubility in oil helps increase the oil saturations in place, and thus improve relative permeability of the oil phase. A total of 25% of the oil present at residual conditions in the damaged zone was recovered from the pre-flush stage. A majority of the oil was produced within 1 PV of pre-flush fluid injection.

3. A proper workflow is to be followed, as presented in this study, to be able to understand the dynamics involved during the pre-flush stage, and to be able to maximize the efficiency of carbonate mineral dissolution and that of oil production. It is advised to inject the pre-flush fluid at the maximum possible injection pressure into the matrix, as high injection rates can aid in directing acid to more efficiently contact carbonate minerals, and the maintenance of high pore pressures can assist the reaction evolved CO_2 to better swell the oil volume in place.

4. XRD techniques do not provide an accurate representation of the mineralogy distribution across the core. It is important to consider this factor, particularly while applying lessons learned from the lab scale at the field scale levels.

Therefore, the importance of consideration of CO_2 in the pre-flush stage analyses has been shown via numerical modeling in concordance with sound experimental studies. It is seldom the case that a single phase environment exists in the damaged zone downhole during the acidizing processes, upon which such an assumption can severely affect the efficacy of a pre-flush stage design. The adopted three-phase approach in this study helps minimize the associated uncertainties, and deliver a more accurate prediction of the pre-flush stage performance.

5.2 Recommendations and Future Work

Although it was proved that the presence of CO_2 has significant effect on the oil present in the near wellbore region, many different case scenarios and experiments were not considered due to lack of time. Future work concerns incorporating those case scenarios so complete understanding of the problem statement can be evaluated. The different case scenarios are mentioned below

1. The coreflood experiments were conducted on non-aged cores, so running coreflood experiments on aged Sandstone cores would further help the understand the effect of CO_2 in pre-flush stage.
2. The distribution of calcite and dolomite mineral in modelling was uniform through out the core, however, it is seldom the case on the field, hence various distribution patterns of carbonate mineral would replicate the downhole conditions.
3. CO2 gas has a well-documented history of incompatibility with asphaltene, hence running experiments with different asphaltene content will add more value to the literature of matrix acidizing.

REFERENCES

1. Abdulagatov, I. M. and Azizov, N. D. 2006. Viscosity of aqueous calcium chloride solutions at high temperatures and high pressures. *Fluid Phase Equilibria.* **240**: 204-219. https://doi-org/10.1016/j.fluid.2005.12.036.

2. Abdelmoneim SS, Nasr-El-Din HA (2015) Determining the optimum HF concentration for stimulation of high temperature sandstone formations. Society of Petroleum Engineers, SPE174203-MS.

3. Aboud RS, Smith KL, Forero Pachon L, Kalfayan LJ (2007) Effective matrix acidizing in high-temperature environments. Society of Petroleum Engineers, SPE 109818-MS

4. Akin, S. and Kovscek, A. R. 2003. Computed Tomography in Petroleum Engineering. *Geol. Soc. Lond.* *Spec. Pub.* **215**: 23-38. http://dx.doi.org/10.1144/GSL.SP.2003.215.01.03.

5. Al-Harthy S (2008/2009) Options for high-temperature well stimulation. Oil Field Rev 20(4):52–62.

6. Bryant, S. L. 1991. An Improved Model of Mud Acid/Sandstone Chemistry. Presented at the SPE Annual Technical Conference and Exhibition, Dallas, Texas. October 6-9. https://doi.org/10.2118/22855-MS

7. Cheng, H., Zhu, D., and Hill, A. D. 2017. The Effect of Evolved CO_2 on Wormhole Propagation in Carbonate Acidizing. *SPE Prod & Oper* **32** (03): 325-332. SPE-178962-PA. https://doi-org/10.2118/178962-PA.

8. CMG-STARS. 2017. *STARS User's Guide*. Calgary, Alberta, Canada: Computer Modeling Group Ltd.

9. Corey, A. T. 1954. The Interrelation between Gas and Oil Relative Permeability. *Producers Monthly* **19** (1): 38-41.

10. Crowe C, Masmonteil J, Touboul E, Thomas R (1992) Trends in matrix acidizng. Oil Field Rev 4(4):24–40.

11. D. Fu. 2010. Self-Diverting Pre-Flush Acid for Sandstone. US Patent No. 7,666,821 B2.

12. Dake, L. P. 1978. *Fundamentals of Reservoir Engineering*, first edition. Amsterdam: Elsevier.

13. Dean, D. E. and Stiel, L. I. 1965. The Viscosity of Nonpolar Gas Mixtures at Moderate and High Pressures. *AIChE J.* **11** (3): 526. https://doi.org/10.1002/aic.690110330

14. Economides MJ, Nolte KG (2001) Reservoir stimulation, 3rd edn. Prentice Hall, Englewood Cliffs.

15. Exler, V. A., Cisneros, F. T., Quevedo, M. A. et al. 2014. Hybrid Matrix Acidizing Techniques Successfully Stimulate Geothermal Wells in Latin America. Presented at the SPE International Symposium and Exhibition on Formation Damage Control, Lafayette, Louisiana. February 26 – 28. https://doi.org/10.2118/168206-MS.

16. Fredd, C. N. and Fogler, H. S. 1999. Optimum Conditions for Wormhole Formation in Carbonate Porous Media: Influence of Transport and Reaction. *SPE J* **4** (03): 196-205. https://doi.org/10.2118/56995-PA.

17. Gomez JN (2006) Design, set-up and testing of a matrix acidizing apparatus. Texas A&M University, Texas.

18. Halliburton (2000a) Carbonate matrix acidizing treatment. Best practice series. Halliburton, Houston.

19. Halliburton (2000b) Effective sandstone acidizing. Best practice series. Halliburton, Houston.

20. Halliburton (2000c) Hydraulic fracturing. Best practice series. Halliburton, Houston.

21. Hekim, Y., Fogler, H. S., and McCune, C. C. 1982. The Radial Movement of Permeability Fronts and Multiple Reaction Zones in Porous Media. *SPE J.* **22** (01): 99-107. https://doi.org/10.2118/9495-PA.

22. Hendraningrat, L., Shidong, Li., and Torsaeter, O. 2013. A coreflood investigation of nanofluid enhanced oil recovery. J. Petroleum Science and Engineering 111 (2013): 128-138. **https://doi-org/10.1016/j.petrol.2013.07.003.**

23. Hill AD, Lindsay DM, Silberberg IH, Schechter RS (1981) Theoretical and experimental studies of sandstone acidizing, SPE-6607- PA.

24. Hill, A. D., Sepehrnoori, K., and Wu, P. Y. 1994. Design of the HCl Preflush in Sandstone Acidizing. *SPE Prod & Fac* **9** (02): 115-120. https://doi.org/10.2118/21720-PA.

25. Kalfayan LJ (2008) Production enhancement with acid stimulation. PennWell, Tulsa

26. Kalfayan LJ, Metcalf AS (2001) Successful sandstone acid design case histories: exceptions to conventional wisdom. Society of Petroleum Engineers, SPE-63178-MS

27. Kumar, H. T., Muhemmed, S., and Nasr-El-Din, H. A. 2019. Compositional Modeling of Carbonate Acidizing Processes with CO_2 Evolution in Aqueous Environments. *SPE J.*

28. Kumar, H. T., Muhemmed, S., and Nasr-El-Din, H. A. 2020. Impact Of Oil Saturation, CO_2 Evolution, And Rock Wettability On Acid Efficiencies During Carbonate Acidizing: A Three-phase Perspective. To be presented at the SPE International Conference and Exhibition on Formation Damage Control, Lafayette, Louisiana, 19—21 February. SPE-199329-MS.

29. Leong, V. H., Ben Mahmud, H., Law, M. C. et al. 2019. A numerical modelling and simulation of core-scale sandstone acidizing process: A study on the effect of temperature. *J. Petroleum Exploration and Production Technology* **9** (1): 483-516. https://doi.org/10.1007/s13202-018-0522-8.

30. Lindsay DM (1976) An experimental study of sandstone acidization. The University of Texas at Austin, Austin.

31. Mahmoud MA, Nasr-El-Din HA, De Wolf C, Alex A (2011) Sandstone acidizing using a new class of chelating agents. Society of Petroleum Engineers, SPE-139815-MS.

32. McLeod, H. O., Jr., Ledlow, L. B., and Till, M. V. 1983. The Planning, Execution, and Evaluation of Acid Treatments in Sandstone Formations. Presented at the SPE Annual Technical Conference and Exhibition, San Francisco, California. 1 January.
33. https://doi.org/10.2118/11931-MS.

34. Nasr-El-Din, H. A., Samuel, M. M., and Kelkar, S. K. 2007. Investigation of a New Single-stage Sandstone Acidizing Fluid for High Temperature Formations. Presented at the European Formation Damage Conference, Scheveningen, The Netherlands. 1 January. https://doi.org/10.2118/107636-MS.

35. Leong, V. H., Ben Mahmud, H., Law, M. C. et al. 2019. A numerical modelling and simulation of core-scale sandstone acidizing process: A study on the effect of temperature. *J. Petroleum Exploration and Production Technology* **9** (1): 483-516. https://doi.org/10.1007/s13202-018-0522-8.

36. McLeod, H. O., Jr., Ledlow, L. B., and Till, M. V. 1983. The Planning, Execution, and Evaluation of Acid Treatments in Sandstone Formations. Presented at the SPE Annual Technical Conference and Exhibition, San Francisco, California. 1 January. https://doi.org/10.2118/11931-MS.

37. McLeod HO Jr, Norman WD (2000) Sandstone acidizing. In: Reservoir stimulation. Wiley, Chichester Muecke TW (1982) Principles of acid stimulation. Society of Petroleum Engineers, SPE-10038-MS.

38. Nasr-El-Din, H. A., Samuel, M. M., and Kelkar, S. K. 2007. Investigation of a New Single-stage Sandstone Acidizing Fluid for High Temperature Formations. Presented at the European Formation Damage Conference, Scheveningen, The Netherlands. 1 January. https://doi.org/10.2118/107636-MS.

39. National Instruments. 2003. LabVIEW, Version 2003 User Guide, Austin, Texas: National Instruments.

40. Ponce da Motta E, Plavnik B, Schechter RS (1992) Optimizing sandstone acidization, SPE-19426-PA

41. Qiu XW, Zhao W, Dyer SJ, Al Dossary A, Khan S, Sultan AS (2014) Revisiting reaction kinetics and wormholing phenomena during carbonate acidising. International Petroleum Technology Conference, Doha, Qatar, pp 15.

42. Redlich, O. and Kwong, J. N. S. 1949. On the Thermodynamics of Solutions V. An Equation of State. Fugacities of Gaseous Solutions. *Chem. Rev.* **44** (1): 233-244. https://doi.org/10.1021/cr60137a013.

43. Reid, R. C., Prausnitz, J. M., and Poling, B. E. 1987. *The Properties of Gases and Liquids*. New York: McGraw Hill.

44. Rivet, S. M., Lake, L. W., and Pope, G. A. 2010. A Coreflood Investigation of Low-Salinity Enhanced Oil Recovery. Presented at the SPE Annual Technical Conference and Exhibition held in Florence, Italy, 19—22 September. SPE-134297-MS. https://doi-org/10.2118/134297-MS.

45. Robinson, D. B. and Peng, D. Y., 1978. The Characterization of the Heptanes and Heavier Fractions for the GPA Peng–Robinson Programs, GPA Research Report RR-28. Gas Processors Association.

46. Sevougian, S. D., Lake, L. W., and Schechter, R. S. 1995. A New Geochemical Simulator To Design More Effective Sandstone Acidizing Treatments. *SPE Prod & Fac* **10** (01): 13-19. https://doi.org/10.2118/24780-PA.

47. Shafiq MU, Kyaw A, Shuker MT (2013) A comprehensive research to find suitable acid for sandstone acidizing. Adv Mater Res 787:274–280

48. Shafiq MU, Shuker MT, Kyaw A (2014) Performance comparison of new combinations of acids with mud acid in sandstone acidizing. RJASET 7(2):323–328

49. Shafiq MU, Mahmud HKB, Hamid MA (2015) Comparison of buffer effect of different acids during sandstone acidizing, IOP conference series: materials science and engineering, vol 78

50. Shafiq et al (2016) New acid combination for a successful sandstone acidizing. Presented in 29th symposium of Malaysian chemical engineers (SOMChE), Miri, Sarawak, Malaysia

51. Shaughnessy, C. M. and Kunze, K. R. 1981. Understanding Sandstone Acidizing Leads to Improved Field Practices. *J Pet Technol* **33** (07): 1196-1202. https://doi.org/10.2118/9388-PA.

52. Shuchart CE (1997) Chemical study of organic-HF blends leads to improved fluids. Society of Petroleum Engineers, SPE-31281- MS Shuchart CE, Buster DC (1995) Determination of the chemistry of HF acidizing with the use of F NMR spectroscopy. Society of Petroleum Engineers, SPE-28975-MS

53. Shuchart CE, Gdanski RD (1996) Improved success in acid stimulations with a new organic-HF system. Society of Petroleum Engineers, SPE-36907-MS.

54. Schechter RS (1992) Oil well stimulation. Prentice Hall, Englewood Cliifs.

55. Schechter, R. S. and Gidley, J. L. 1969. The change in pore size distribution from surface reactions in porous media. *AIChE Journal* 15 (3): 339-350. https://doi.org/10.1002/aic.690150309.

56. Schlumberger (2000) Reservoir stimulation. Wiley, Chichester.

57. Smith CF, Hendrickson AR (1965) Hydrofluoric acid stimulation of sandstone reservoirs, SPE-980-PA.

58. Teledyne ISCO. 2018. D-Series Pumps, Version 2018 User Guide. Lincoln, Nebraska: Teledyne ISCO.

59. Thomas RL, Nasr-El-Din HA, Lynn JD, Mehta S, Zaidi SR (2001) Precipitation during the acidizing of a HT/HP illitic sandstone reservoir in eastern Saudi Arabia: a laboratory study. Society of Petroleum Engineers, SPE-71690-MS

60. Thomas RL, Nasr-El-Din HA, Mehta S, Hilab V, Lynn JD (2002) The impact of HCl to HF ratio on hydrated silica formation during the acidizing of a high temperature sandstone gas reservoir in Saudi Arabia. Society of Petroleum Engineers, SPE-77370-MS

61. Williams, Bert B., Gidley, J. L., Schechter, R. S. et al. 1979. *Acidizing fundamentals,* 124 pages : illustrations; 28 cm. New York: Henry L. Doherty Memorial Fund of AIME, Society of Petroleum Engineers of AIME.

62. Zhao, H., Fedkin, M. V., Dilmore, R. M. et al. 2015. Carbon dioxide solubility in aqueous solutions of sodium chloride at geological conditions: Experimental results at 323.15, 373.15, and 423.15 K and 150 bar and modeling up to 573.15 K and 2000 bar, Geochimica et Cosmochimica Acta 149: 165-189. https://doi-org/10.1016/j.gca.2014.11.004

63. Zhixue, S., Zhilei, S., Hongjiang, L. et al. 2010. Characteristics of carbonate cements in sandstone reservoirs: A case from Yanchang Formation, middle and southern Ordos Basin, China. *Petroleum Exploration and Development* **37** (5): 543-551. https://doi.org/10.1016/S1876-3804(10)60054-7.

64. Yang F, Nasr-El-Din HA, Al-Harbi BM (2012) Acidizing sandstone reservoirs using HF and formic acids. Society of Petroleum Engineers, SPE-150899-MS

65. Zimmerle, W. 1995. *Petroleum sedimentology*. Dordrecht: Kluwer Academic Publishers.